이학박사 학위논문

전이성 유방암 환자 유래 생검조직 이식 동물모델의 수립 및 유전체 분석

Genomic profile of metastatic breast cancer patient-derived xenografts established using biopsy sample

2021년 2월

서울대학교 대학원

협동과정 종양생물학 전공

김 선 경

전이성 유방암 환자 유래 생검조직 이식 동물모델의 수립 및 유전체 분석

지도교수 임 석 아

이 논문을 이학박사 학위논문으로 제출함.

2020년 10월

서울대학교 대학원

협동과정 종양생물학 전공

김 선 경

김 선 경의 이학박사 학위논문을 인준함.

2021년 1월

위 원 장 전 윤경 (인)

부위원장 임 석 아 (인)

위 원 김 동완 (인)

위 원 김 지현 (인)

위 원 박 연희 (인)

Genomic profile of metastatic breast cancer patient-derived xenografts established using biopsy sample

by

Seongyeong Kim

(Directed by Seock-Ah Im, M.D., Ph.D.)

A Thesis Submitted to the Interdisciplinary Graduate Program in Partial Fulfillment of the Requirements for the Degree of Doctor of Philosophy in Cancer Biology at the Seoul National University, Seoul, Korea

January, 2021

Approved by thesis committee:

Professor Yoon Kyung Jeon Chairperson

Professor Seock-Ah Im Vice Chairperson

Professor Dae-Wan Kim

Professor Jee Hyun Kim

Professor YEON HEE PARK

ABSTRACT

Genomic profile of metastatic breast cancer patient-derived xenografts established using biopsy sample

Seongyeong Kim

Major in Cancer Biology

Interdisciplinary Graduate Program

The Graduate School

Seoul National University

Background: Metastatic breast cancer is a complex and life-threatening disease, although it is hard to cure, patients can get survival benefit from sequential anti-cancer treatment. Patient-derived xenograft (PDX) model is suggested as a practical tool to predict the clinical outcome of cancer treatment as well as to screen novel drugs. This study aimed to establish PDX models in Korean patients and analyze their genomic profiles and the utility for

translational research.

Methods: Percutaneous core needle biopsy or punch biopsy samples were used for xenotransplantation. The tumor tissue which has grown in the mouse was used for genome analysis. Whole exome sequencing and transcriptome analysis were performed to assess the genomic and RNA expression profiles, respectively. Copy number variation (CNV) and mutational burden were analyzed and compared with other metastatic breast cancer genomic results. The medical records were reviewed to understand the clinico-pathologic characteristic of enrolled patients. Moreover, the antitumor effect of an ATR inhibitor was tested in the relevant PDX model.

Results: Of the 151 cases enrolled in this study, 40 (26%) PDX models were established. Notably, the take rate of all subtype, including hormone receptor-positive (HR+) subtype, exceeded 20%. The PDX model had genomic fidelity and CNV that represented the pattern of its donor sample. The somatic mutations of *TP53, PIK3CA, ESR1*, and *GATA3* were frequently found. *ESR1* mutation, *CCND1* amplification, and APOBEC signature were significant features in HR+ HER2− PDX model. Fulvestrant in combination with palbociclib showed partial response to the relevant patient' s tumor harboring *ESR1* mutation and *CCND1* amplification found in PDX model. AZD6738, an ATR inhibitor, presented delayed

tumor growth in a relevant PDX model.

Conclusions: PDX model is well established using core needle biopsy samples from primary and metastatic tissues. Genomic profiles of the samples reflected their original tissue characteristics and could be used for the interpretation of clinical outcomes. These findings can increase the utility of this model in translational research.

Keywords: Metastatic breast cancer, Patient-derived xenograft, Whole exome sequencing, Translational research, Korean PDX model.

Student Number: 2014-31286

TABLE OF CONTENTS

LIST OF TABLES

LIST OF FIGURES

INTRODUCTION

Breast cancer is the most prevalent cancer in women. To conquer breast cancer, numerous studies have described various approaches to treat this disease; however, in the case of patients with metastatic breast cancer (mBC), the 5-year survival rate is still below 40% (1). To break through this huddle, precision medicine was emerging for better matching of the drug to the patient. In breast cancer, treatment decisions are largely based on three well-classified molecular markers, hormone receptors (HR) including estrogen receptor (ER) and progesterone receptor (PR) and human epidermal growth receptor 2 (HER2). However, these clinical molecular subtyping based on immunohistochemistry (IHC) are insufficient and the precise molecular markers are needed to select better drugs for each patient and to implement precision medicine (2). Moreover, the tumor heterogeneity in breast cancer patients results in differences in the same subtype (3). Due to the insufficient molecular markers and drug resistance, various chemotherapeutic drug combinations used for the treatment of mBC have been unsuccessful (4). Thus, there is an eager need to identify novel molecular markers using better technique and understand the characteristics of the individual tumor.

Patient-derived xenograft (PDX) models are known to

provide a more accurate reflection of tumor biology than cell lines (5). Previous studies have reported that established PDX models retain the histological and genetic characteristics of their donor tumor; therefore, it is assumed that this model has the potential to predict clinical outcomes and can be used for newly developed drug screening (6). Moreover, the PDX model is also utilized for precision medicine and therapeutic marker discovery. The key technology for precision medicine is high-resolution sequencing, and the genome data obtained from it could provide an insight to understand each tumor and to select for precise treatments. The sequencing technology is advanced remarkably, the quantity and quality of specimens are still an issue. In the case of mBC patients, it is not easy to obtain a sufficient amount of tumor tissue for multiple analyses thus it is needed to the practical use of the patient' s tissue for cancer treatment and well fare of the patient. The establishment of the PDX model can be a practical solution. Despite these advantages, the PDX model also has a few limitations. Primary surgical tissues were preferred to engraft the PDX model because the cancer cell population of tissue is high and gets lots of tumor tissues for implantation. There is a limitation of collecting surgical tissues of mBC patients, thus, PDX models using metastatic tissues are scarce. In metastatic cancer, the biopsy performs for diagnosis but tumor cell density might low and the

amount of tissue is not enough for further test or implantation. The take rate exceeds 50% in triple-negative breast cancer, which is an aggressive subtype; in contrast, the take rate in ER or PR-positive subtype, which is relatively indolent, is usually less than 10% (6, 7). In addition, there are still disparities in ethnic and racial distributions. In previous studies, most PDX models were established from Caucasian women, followed by Afro-American and Hispanic women (8). PDX models from Asian breast cancer patients are relatively scarce and their characteristics are underrepresented.

In this study, 40 PDX models were established using percutaneous biopsy samples from Korean patients with mBC. The overall take rate was 27%. The histological and genomic profile of the patient tumor and engrafted PDX tissues were analyzed to verify the similarity between the PDX model and donor tissue. After the PDX establishment, the tumor tissues were analyzed using whole-exome sequencing (WES) to assess the mutation and copy number variation (CNV) pattern. Moreover, to evaluate the potential use of PDX in translational research, the genomic information from the PDX models were used to decide the selection of drugs for some patients. The anti-tumor activity of the inhibitor of Ataxia telangiectasia and Rad3 related (ATR) were explored in relevant models.

MATERIALS AND METHODS

1. Patient recruitment and tissue collection

The patients diagnosed with locally advanced or mBC were enrolled in this study for PDX establishment and genomic profiling from 2014 to 2017. The patient tissues of primary breast or various metastatic sites were acquired by percutaneous core needle biopsy or punch biopsy and put into the RPMI 1640 tissue culture medium (Thermo Fisher Scientific Inc., Waltham, MA, USA) supplemented with 10 U/ml penicillin and 10 μg/ml streptomycin. The maximum portion of the tissue was used for mice transplantation, whereas the remaining was used for genetic analysis. The study protocol was approved by the Institutional Review Board of the Seoul National University Hospital (SNUH) (IRB No: 1402-054-555).

2. Establishment of PDX mouse model

The xenograft experiment was performed after approval from the Institutional Animal Care and Use Committee. NOD.Cg-*Prkdc*^{scid} *Il2rg*^{tm1Wjl}/SzJ (NSG) mice were purchased from Jackson Laboratories (Bar Harbor, ME, USA). Fresh biopsy tissue was prepared within 30 minutes and

was implanted into the mammary fat pad of near left leg of NSG mouse within 1 hour. The mouse was monitored until the tumor reached a size of 200 mm^3 or for 6 months. When the xenograft tumor size exceeded 200 mm^3, we operated the mice, and the tissue fragments were transplanted into other mice to increase the number of tumor-bearing mice or were preserved in liquid nitrogen for future engraftment. A part of the tumor tissue was fixed in formalin for pathological analysis and the remaining portion was preserved for genomic analysis.

Each sample was named with the following order. 'IMT_' or 'T_' stands for patient tumor sample, 'IMX_' or 'X_' stands for PDX tumor sample.

3. DNA extraction, library preparation, and genome analysis

Genomic DNA was extracted using the frozen tissue. Genomic DNA from PDX and patient biopsy tissues were prepared by DNeasy Blood and Tissue Kit (Qiagen, Hilden, German). Genomic DNA from the patient blood sample was prepared by Qiagen Gentra Puregene Blood Kit. Agilent SureSelectXT Human All Exon V5 (Agilent technology Inc., CA, USA) was used for DNA library preparation. All experiments were performed according to the

manufacturer’s instructions.

WES was performed using HiSeq platform (Illumina). WES reads were mapped to the combined reference for human GRCh19 and mouse mm10 genome versions using BWA (9). We used a combined reference as mixed samples of different species could be found. Multiple-mapped reads were discarded because they are likely to span human and mouse references. Then, we split bam files using human reference to obtain human-unique reads. Additional pre-processing followed the recommendations of Genome Analysis Tool Kit (GATK) (10).

The mean depth of our sequencing data was 150X in tumor tissue of patient and PDX, 100X in the blood sample. The samples achieved average of 97.87% of the targeted exome bases covered to a depth of 10X or greater.

4. Variant calling and copy number alteration analysis

Single nucleotide polymorphisms (SNPs) and small insertions and deletions (Indels) were analyzed using muTect (1.1.7) and IndelGenotyper provided by GATK (3.6.0), respectively (11). Variants with at least four read depths were selected and the nonsilent somatic mutation was assessed using an in-house filtering method (Total

depth ≥ 4, exonic splicing, or nonsynonymous SNV or Frameshift InDel or population DB frequencies ≤ 0.01). Additionally, various population study databases (ExAC (Exome aggregation consortium) (12), esp6500 (Exome Sequencing Project v. 6500) (13), and 1000 genome project (14)) were used to filter out common variants. The germline mutations were distinguished by paired sequencing of blood samples. Moreover, it was investigated whether the CNVs were maintained in the PDX models. CONIFER (15) was used for enumerating the read fragments in WES data. The logarithm of blood and tumor sample sequencing data was used for CNV analysis, and the somatic CNVs were segmented with a "DNA copy." B allele frequencies (BAF) were selected by Mutect and visualized by Integrative Genomics Viewer (IGV).

5. Mutational signature analysis

The mutational signature was analyzed using DeconstructSig (16) that allows individual analysis of each sample. The mutation fractions were calculated from the somatic mutations from each sample. Extracted signatures were characterized based on 96 trinucleotide contexts. To efficiently distinguish the signature, cosine similarity was obtained by comparison with the COSMIC signatures (17).

6. RNA sequencing and normalization

The tumor tissues obtained from PDX were used for transcriptome sequencing. TruSeq v2 was used in the RNA library preparation (TruSeq RNA Library Prep Kit v2, illumina inc., CA, USA). Transcriptome sequencing data were mapped to the same reference for WES using a STAR aligner (18). The following processing was performed as the Best Practices workflow for RNA-seq using GATK. Gene expression levels were quantified for BAM files by fragments per kilobase of exon per million mapped reads (FPKM) using HTSeq-count (19).

The transcriptome data was used for subtyping the PDX samples into 4 subtypes (luminal A, luminal B, HER2-enriched, and basal like) according to the previous methods (20).

7. Differential expressed gene and ontology analysis

The DESeq2 algorithm was used to determine the expression level change between *ESR1*-mutant and wild type in the HR+ samples (21). G:Profiler, which is a web-based tool was used to evaluate the ontology to identify the different pathways and their mechanisms (22) and REVIGO was used to reduct ontologies (23).

8. PDX drug study

AstraZeneca provided AZD6738, an ATR inhibitor. This drug was administered by oral gavage once daily at a concentration of 50mg/kg for 4 weeks. The tumor was measured every other day using calipers, and the volume was calculated with the following formula: $[(\text{width})^2 \times (\text{height})]/2$. Following 4 weeks of drug treatment, the mice were monitored to assess the mouse tumor growth.

RESULTS

1. The characteristic of the PDX study enrolled patient

In total, 151 core needle biopsy tissues were obtained from 130 patients between 2014 and 2017 for the establishment of PDX. The enrolled patients presented locally advanced breast cancer or mBC during tissue collection. Of the 151 tissues, 38 were collected from the primary breast tumor site and 113 originated from various metastatic tissues. The liver tissues were the most frequent metastatic tissue and lymph node, lung, soft tissue, bone, skin, brain, and fluid were used for PDX establishment.

The distribution of tumor subtype based on ER, PR, and HER2 expression was determined by IHC, in the clinic. The HR+ HER2- subtype was most common (64/151, 42.4%), whereas the prevalence of HR+ HER2+ type was the lowest (18/151, 11.9%). Most of the tumor histologic type was infiltrating ductal carcinoma (IDC, 140/151, 92.7%), 7 (4.6%) were invasive lobular carcinoma (ILC), 3 (2.0%) represented a mixture of IDC and ILC, and 1 (1.3%) case was Metaplastic carcinoma with matric-producing and squamous cell carcinoma (Table 1).

The individual information of the patient characteristics

matched with the established PDX model is presented in table 2. The models were organized by the subtype based on IHC and the biopsy site of tissue, histologic subtype, and treatment history for metastatic disease before the biopsy for implantation was indicated (Table 2). Adjuvant and neoadjuvant therapy were not described and were not counted as previous lines of therapy in this table. The median number of previous lines of therapy was 3 (range 0-9) before the implantation of the tumor.

Table 1. Characteristic of PDX enrolled specimen

Characteristic	Number of Samples N=151*(%)
Age (years)	
Median (range)	53 (28-78)
Biopsy site of origin	
Primary site (Breast)	38 (25%)
Metastatic site	113 (75%)
Tumor Subtype	
HR+ HER2-	64 (42.4%)
HR+ HER2+	18 (11.9%)
HR- HER2+	28 (18.5%)
TNBC	41 (27.2%)
Histologic Subtype	
Invasive ductal carcinoma	140 (92.7%)
Invasive lobular carcinoma	7 (4.6%)
Mixed ductal and lobular cancer	3 (2.0%)
Metaplastic carcinoma with matric -producing and squamous cell carcinoma	1 (1.3%)

* The enrolled patient number is 130

Table 2. Characteristic of established PDX model and the prior therapy history

Patient tissue Subtype	Sample	Biopsy site	Histologic subtype		Therapy
HR+ HER2-	X108	liver	IDC	2	Trastuzumab (Herceptin™)+Lapatinib+Letrozole (Femara™) Trastuzumab (Herceptin™)+Docetaxel+Zoledronic acid
	IX_29	liver	IDC	3	weekly Paclitaxel+Zoledronic acid Tamoxifen+Zoledronic acid GnRHa (Zoladex™)
	IMX_37	liver	IDC	3	Docetaxel+Cyclophosphamide Letrozole (Femara™)+Zoledronic acid Exemestane (Aromasin™)+Everolimus (Afinitor™)+Zoledronic acid
	IMX_62	breast	IDC	1	Gemcitabine +Paclitaxel
	IMX_80	breast	IDC	0	
	IMX_135	liver	mixed IDC and lobular cancer	4	Tamoxifen Gemcitabin+Paclitaxel Letrozole (Femara™) Fulvestrant (Faslodex™)+Zoledronic acid
	IMX_151	lymph node	ILC	2	Tamoxifen Talazoparib (BMN673-301)
	IMX_154	Sternum soft tissue	IDC	1	Anastrozole (Arimidex™)
	IMX_158	liver	IDC	3	Letrozole (Femara™)+Zoledronic acid Exemestane (Aromasin™)+Everolimus (Afinitor™) Exemestane (Aromasin™)
	IMX_163	liver	IDC	4	Tamoxifen Fulvestrant (Faslodex™)+Zoledronic acid Gemcitabin+Paclitaxel Zoledronic acid
	IMX_166	breast	IDC	2	Docetaxel+Zoledronic acid Capecitabine (Xeloda™)+Cisplatin
	IMX_181	breast	IDC	9	Exemestane (Aromasin™) Eribulin Capecitabine (Xeloda™) Capecitabine (Xeloda™)+Cisplatin AZD1775+Carboplatin Docetaxel Fulvestrant (Faslodex™) Vinorelbine Olaparib+ATM inhibitor (AZD0156)
HR+ HER2+	X145	liver	IDC	4	Letrozole (Femara™) Lapatinib+Capecitabine (Xeloda™) Vinorelbine Margetuximab (MGAH22)
	X89	skin	IDC	4	Paclitaxel+Trastuzumab (Herceptin™) Lapatinib+Capecitabine (Xeloda™) LJM716 Margetuximab (MGAH22)
	IMX_57	skin	IDC	3	Trastuzumab (Herceptin™)+Lapatinib+Letrozole (Femara™) Margetuximab (MGAH22) Zoledronic acid
	IMX_161	skin	IDC	0	

(Continue to the next page)

Patient tissue Subtype	Sample	Biopsy site	Histologic subtype		Therapy
HR- HER2+	X157	lymph node	IDC	3	Lapatinib+Capecitabine (Xeloda™) Vinorelbine Gemcitabine+Cisplatin
	IMX_49	Pericardial	IDC	5	Trastuzumab (Herceptin™)+LJM716 Vinorelbine Eribulin Gemcitabine+Cisplatin T-DM1
	IMX_58	breast	IDC	3	Lapatinib+Capecitabine (Xeloda™) Margetuximab (MGAH22) Vinorelbine
	IMX_65	peritoneal	IDC	3	Paclitaxel+Trastuzumab (Herceptin™)+Zoledronic acid Lapatinib+Capecitabine (Xeloda™) Gemcitabine+Zoledronic acid
	IMX_76	lymph node	IDC	3	Trastuzumab (Herceptin™)+Vinorelbine Lapatinib+Capecitabine (Xeloda™) Poziotinib
	IMX_79	Lymph node	IDC	0	
TNBC	X98	Lymph node	IDC	1	Vinorelbine+Cisplatin
	X151	breast	IDC	0	
	IX_35	Lymph node	IDC	3	Capecitabine (Xeloda™) Vinorelbine Eribulin
	IMX_41	lung	IDC	0	
	IMX_46	Lymph node	IDC	0	
	IMX_87	breast	IDC	2	weekly Paclitaxel+/-Bevacizumab Irinotecan+Capecitabine (Xeloda™)
	IMX_90	breast	IDC	0	
	IMX_106	breast	IDC	0	
	IMX_107	liver	IDC	0	
	IMX_165	breast	IDC	3	Nab-Paclitaxel+/-Atezolizumab Doxorubicin+Cyclophosphamide Vinorelbine
	IMX_172	breast	IDC	5	Fulvestrant (Faslodex™) Gemcitabine+Paclitaxel Capecitabine (Xeloda™) Pembrolizumab MK3475 KN119 trial Olaparib
	IMX_186	breast	IDC	2	Capecitabine (Xeloda™) Pemetrexed+Vinorelbine

2. Established PDX model was concordant with the origin tissue

The take rate of the PDX model was 26% (40/151). To understand different take rate according to the subtype, PDX models were subdivided according to the tissue subtype. Notably, the take rate of all subtypes exceeded 20% (Figure 1). The triple-negative breast cancer (TNBC) subtype presented the highest take rate (34%). Especially, HR+ HER2- subtype is well established with take rate of 22%. The established PDX model using primary tissues presented a better take rate than that using metastatic tissues (37% vs. 23%) despite the absolute case numbers being higher in the metastatic model (Figure 2). Various metastatic tumor tissues were used to establish the PDX model and the take rate differed among the metastatic site although some tissues were less than 7 cases (Table 3). Whether the degree of Ki-67 expression of donor's tissue is relevant to the PDX take rate was further analyzed. Among 151 cases, 85 cases were available for the Ki-67 index for the patients' tissue analysis. Samples were divided into two groups based on the median value of the degree of Ki-67 expression, 15. The take rate was more than twice in the group of 15 and above compare to the other (Figure 3).

The histological and genomic characteristics were examined to check the fidelity between the PDX tumor and

donor tissue. The information of ER, PR, and HER2 expression of donor's tissue was acquired by the clinical record and the marker expression of the PDX model was analyzed by IHC (Figure 4A). The histological characteristics were about 90% concordant between the patient and PDX tumors (Figure 4B). WES was performed using established PDX tumors and some patient tissues. The somatic mutation pattern was inspected to confirm the similarity between the PDX model and patient tissue (Figure 5). This result demonstrated that the PDX and patient genomes presented considerably identical mutations. Whether the CNVs were altered in the PDX model was further analyzed. As presented in figure 6, the overall CNV patterns were well correlated between the origin tissue and PDX model. These results indicated that metastatic breast PDX model has a high fidelity compared with its origin.

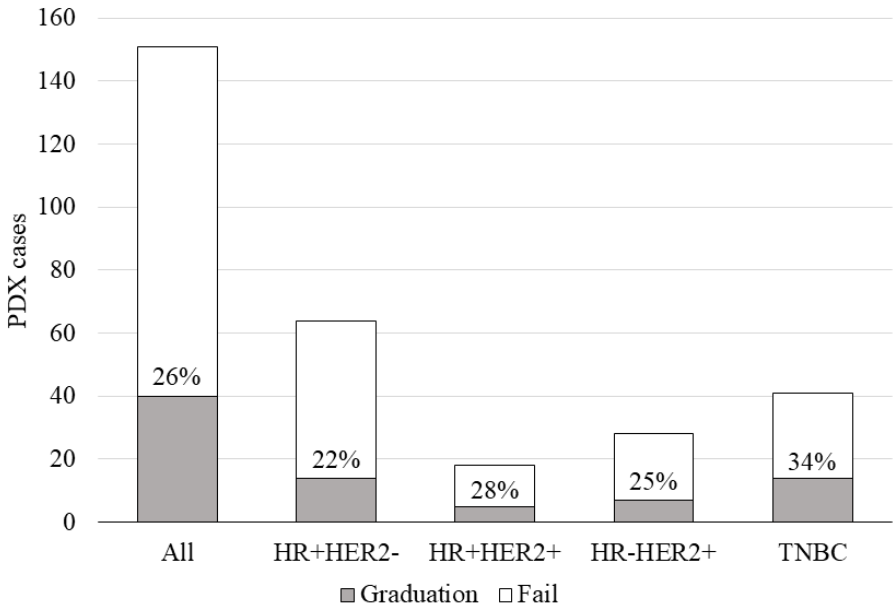

Figure 1. The PDX take rate of our PDX model.

The take rate of PDX model was analyzed and indicated with a bar graph. The overall take rate and take rate by subtype classification based on IHC were analyzed. Each bar graph indicates the sample numbers. The empty bar means fail cases and gray filled bar means graduation cases.

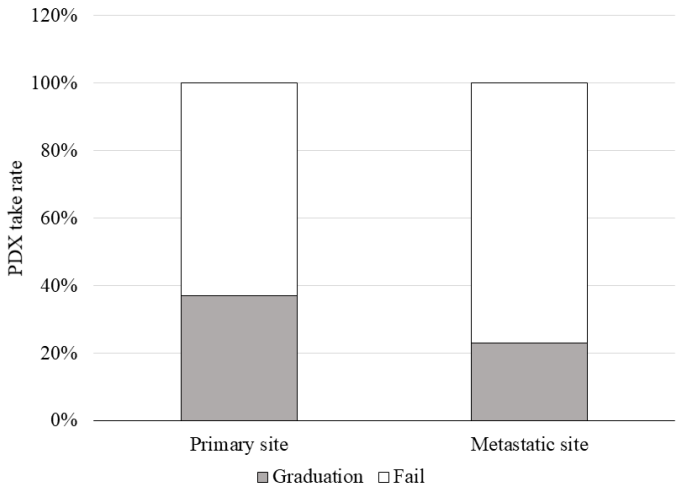

Figure 2. The take rate of the PDX model based on the biopsy tissue type.

The take rate of the PDX model was analyzed by the biopsy tissue site. The empty bar means fail cases and gray filled bar means graduation cases.

Table 3. The PDX model take rate by biopsy site

Biopsy site	Take rate % (Graduation/Total)
Primary site	
Breast	36.8 (14/38)
Metastatic site	
Liver	20.0 (9/45)
Lymph node	25.8 (8/31)
Lung	14.3 (2/14)
Skin and soft tissue	45.5 (5/11)
Bone	0.0 (0/6)
Brain	0.0 (0/2)
Peritoneal seeding	50.0 (1/2)
Pericardium	50.0 (1/2)

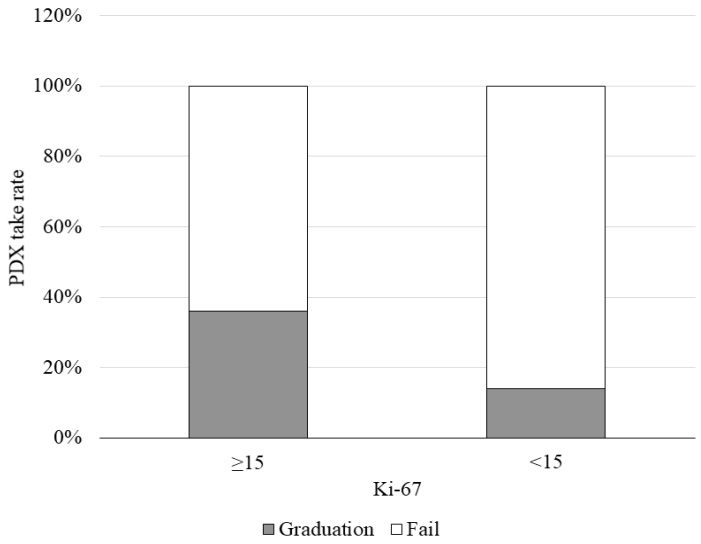

Figure 3. The take rate of the PDX model by the Ki-67 index.

The sample was divided into two groups based on the median value of the degree of Ki-67 expression, 15. Then, the take rate was analyzed and indicated with a bar graph. The empty bar means fail cases and gray filled bar means graduation cases.

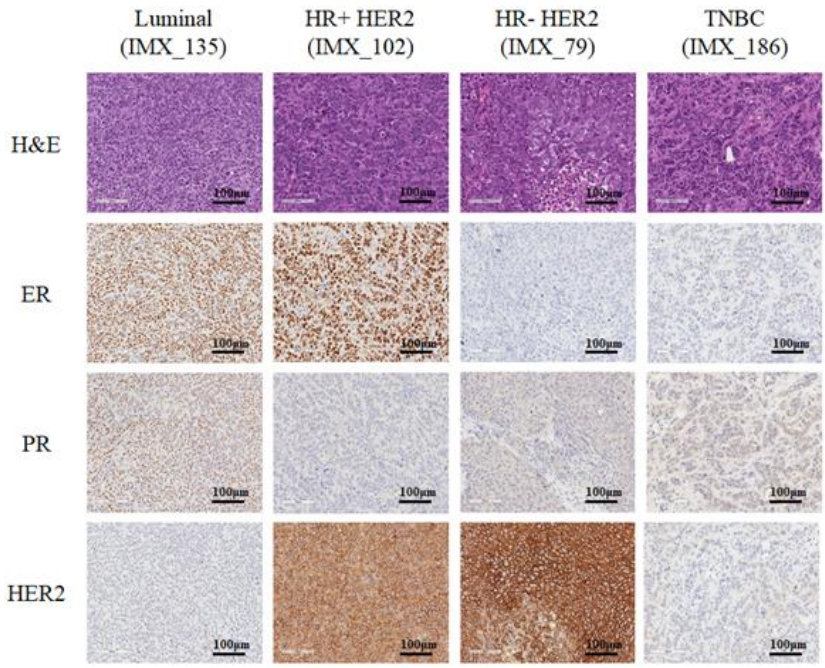

Figure 4. The comparison of histologic characteristic of the PDX model tissue and the donor patient tissue.

A. The IHC result of established PDX tumor tissue. Each model's name and the donor's subtype were written at the top of the figure and the figures below the model's name were the IHC results of matched PDX tumors.

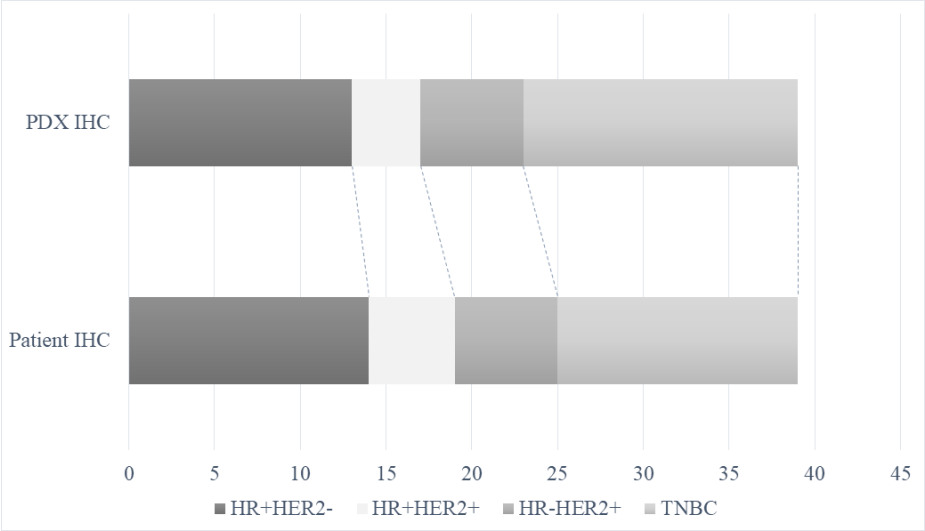

Figure 4. B. The number of PDX or patient donor cases matched with each subtype was indicated with the bar graph. The upper bar is the case number of the PDX model and the bottom bar is the case number of donor cases. The dotted line links the same subtype.

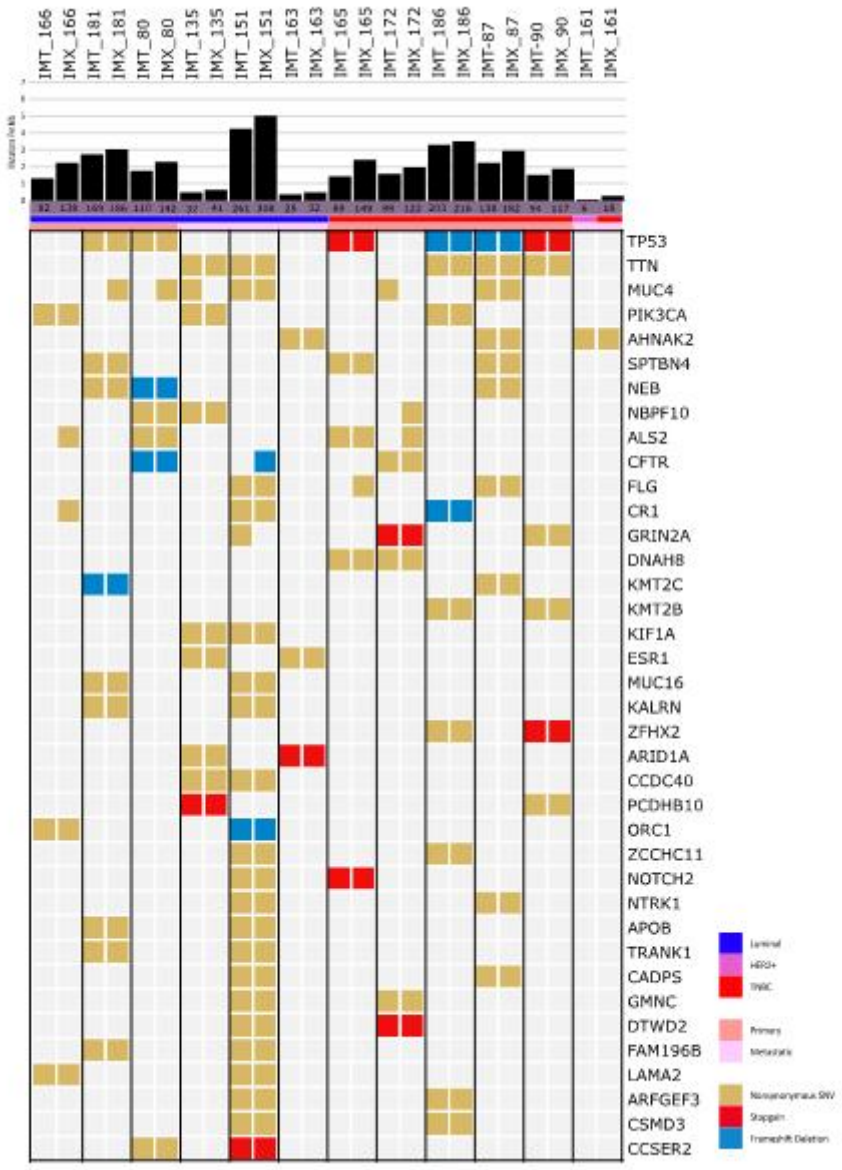

Figure 5. The comparison of somatic mutation patterns between PDX tumors and donor tumors.

The somatic mutation patterns of the patient tissue and its matching PDX model. The case number with IMT indicates that it is the result of patient tissue analysis and the case number with IMX depicts the result of PDX tissue analysis. The subtype and tissue type were indicated by the color bar below the sample name. The mutation types were also classified by the color.

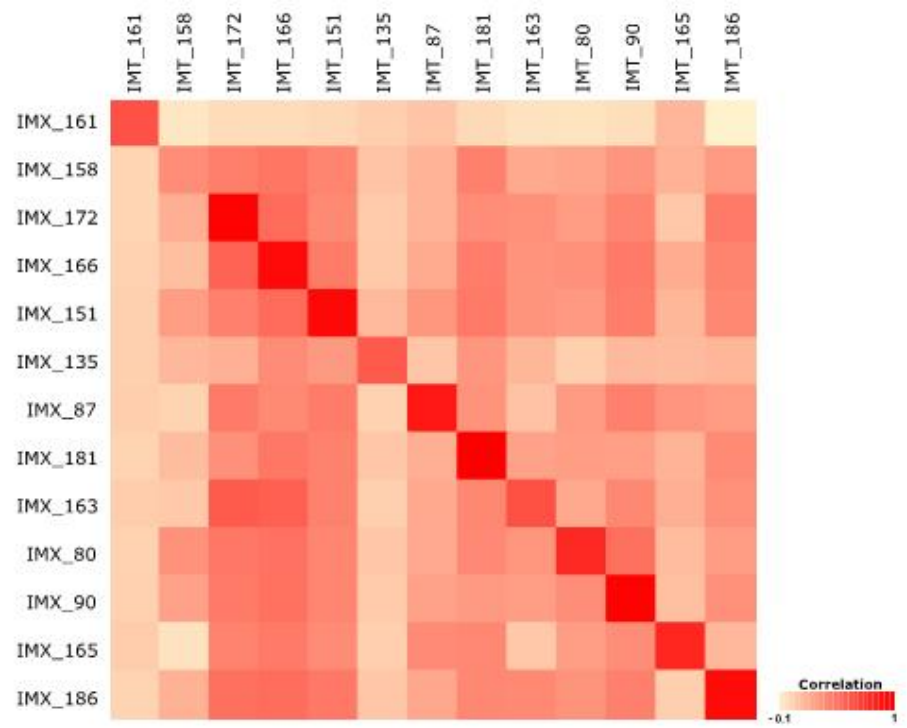

Figure 6. Copy number variation concordance between patient and PDX tissue.

The patient samples placed on the horizontal axis and the PDX samples placed on the vertical axis. The correlation was determined by Person correlation analysis using the log2 fold change value of each sample. The concordance of the CNV is indicated by the color.

3. Genomic alteration of PDX samples

The genomic variation of the PDX sample was analyzed using WES. 6,094 non-silent mutations led to insertions and deletions. The range of non-silent mutation count varied from 24 to 631 in individual samples. Next, the mutated gene list was aligned from high to low frequencies (Figure 7). The *TP53* was the most mutated gene among samples. The frequency of the mutation rate was 64.7% which is higher compare with the TCGA data using surgical tissue for analysis (24). Unlike *TP53*, the mutation rate of other genes did not exceed more than 20%. The frequency of *PIK3CA* mutations was 17.6%, while that of *ESR1, GATA3,* and *GRIN2A* mutations was 14.7% in the overall samples.

To compare the features of PDX established from metastatic biopsy samples, the public datasets "the metastatic breast cancer project (25)" and "the SAFIR01, SAFIR02, SHIVA, or Molecular Screening for Cancer Treatment Optimization (MOSCATO) prospective trials (26)" were analyzed and compared with our data. The mutation frequency of *TP53* and *ESR1* genes was higher in the SNU PDX model, but *PIK3CA* mutations were relatively low (Figure 8A). To eliminate the sample size differences of each subtype in the individual dataset, the mutation frequency of three representative genes from each dataset was compared,

according to the subtypes. As presented in Figure 8B, the *TP53* and *ESR1* mutations were significantly higher in the SNU PDX model compared to *PIK3CA* and other datasets. The mutation burden of this model was significantly higher compared with other datasets (Figure 9). While comparing the allele frequencies between the patient and PDX tumors, the germline and somatic alterations in breast cancer-related genes were stably conserved and amplified in the PDX tumors (Figure 10).

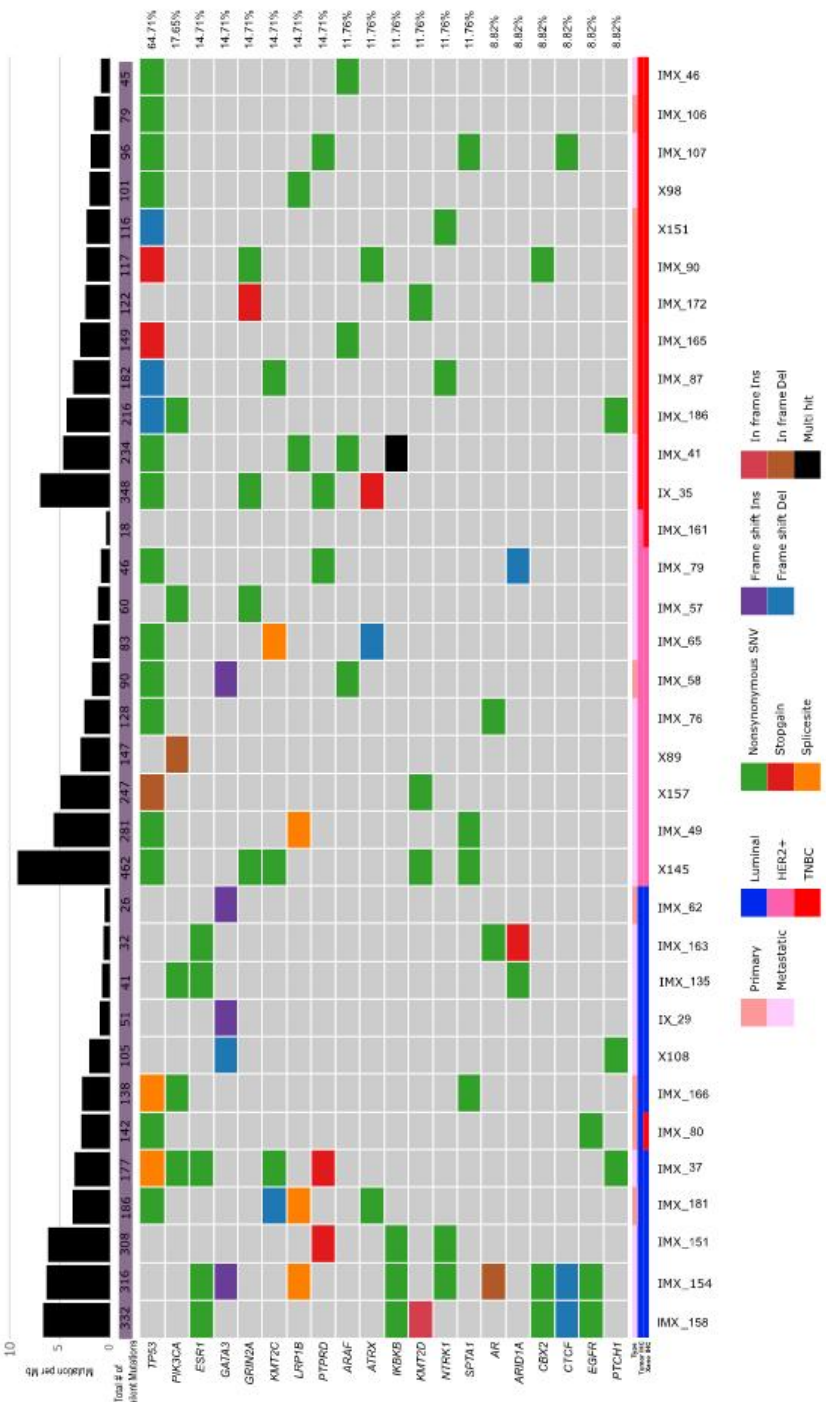
64.71%
17.65%
14.71%
14.71%
14.71%
14.71%
14.71%
14.71%
14.71%
11.76%
11.76%
11.76%
11.76%
11.76%
11.76%
8.82%
8.82%
8.82%
8.82%
8.82%
8.82%
Mutation per Mb
Total # of Non-silent Mutations
TP53
PIK3CA
ESR1
GATA3
GRIN2A
KMT2C
LRP1B
PTPRD
ARAF
ATRX
IKBKB
KMT2D
NTRK1
SPTA1
AR
ARID1A
CBX2
CTCF
EGFR
PTCH1
Tissue Type
Tumor Grade
IMX_46
IMX_106
IMX_107
X98
X151
IMX_90
IMX_172
IMX_165
IMX_87
IMX_186
IMX_41
IX_35
IMX_161
IMX_79
IMX_57
IMX_65
IMX_58
IMX_76
X89
X157
IMX_49
X145
IMX_62
IMX_163
IMX_135
IX_29
X108
IMX_166
IMX_80
IMX_37
IMX_181
IMX_151
IMX_154
IMX_158
In frame Ins
In frame Del
Multi hit
Frame shift Ins
Frame shift Del
Nonsynonymous SNV
Stopgain
Splicesite
Luminal
HER2+
TNBC
Primary
Metastatic

Figure 7. The Somatic mutation pattern of PDX model.

Somatic mutation in our PDX model was aligned according to frequency. Samples were placed on the horizontal axis ordered by subtype. The subtype, biopsy site, and mutation type were indicated by the color.

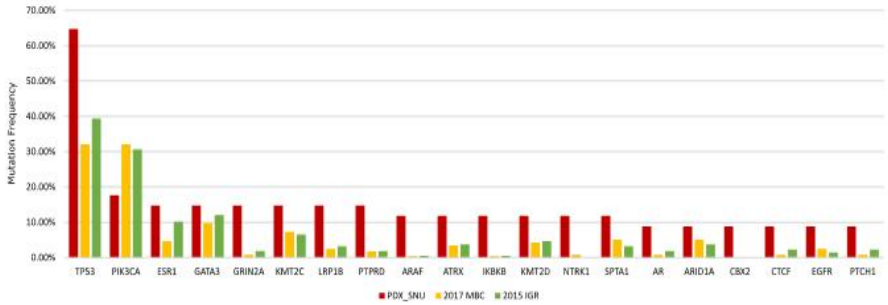

Figure 8. The significant of *ESR1* and *TP53* mutations in the SNU PDX model.

A. The mutation frequency of each gene was indicated by a bar graph. The horizontal axis ordered by the mutation frequency in the SNU PDX model.

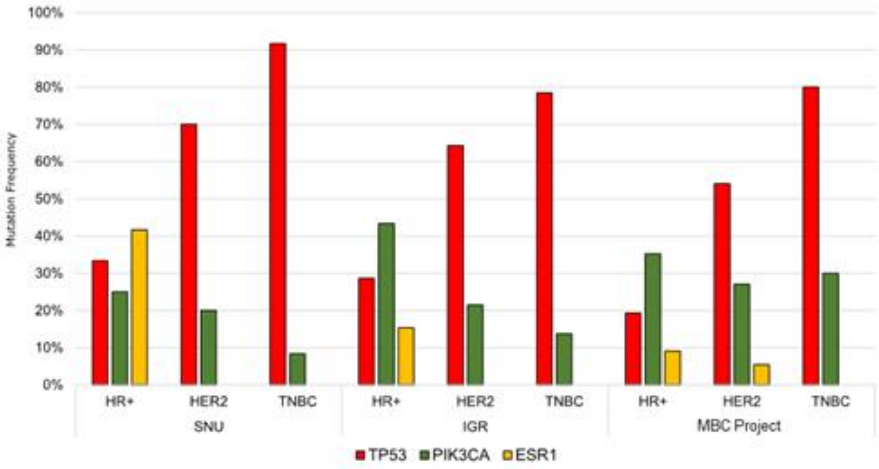

B. The mutation frequency of *TP53, PIK3CA*, and *ESR1* was analyzed by its subtype and represented in a bar graph compared with the other datasets

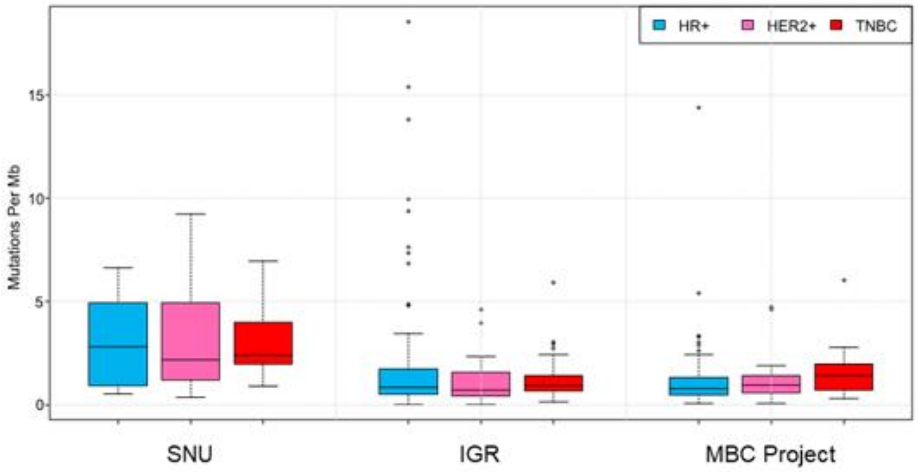

Figure 9. The comparison of mutation burden of the PDX model and public dataset.

The comparison between the PDX model and references of the mutation burden by subtype. The data were analyzed by the subtype to compensate for the differences in the sample size.

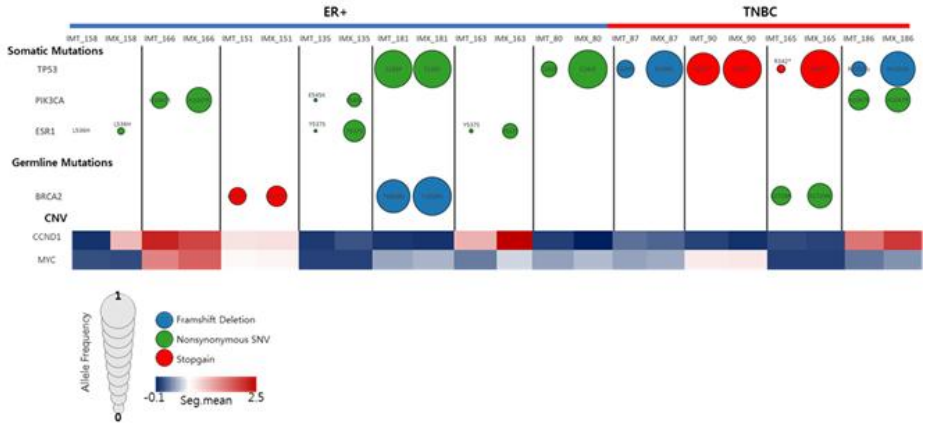

Figure 10. The strengthened of allele frequency of somatic mutations in the PDX model.

The mutation frequency of actionable mutation genes was presented. The mutation that was detected in the patient and PDX tumor samples derived from the same patient was compared. The allele frequency of somatic mutation was strengthened in the PDX model compared with patient tissue.

4. The pattern of copy number variation in the PDX model

The copy number variation of the PDX sample was analyzed by WES data to examine whether the significant structural variation was observed in the PDX genome. As shown in figure 11, the deletion of genes was observed across almost all chromosomes. Unlike this, the amplification of genes was focused on certain chromosomes such as chromosome number 2, 8, 11, and 17. To further analyze, we divided this data based on the tissue subtype and checked the CNV patterns differences. The HR+ subtype, the amplification of chromosome 11 was noticed where the *CCND1* and *FGF* genes located (Figure 12A). The amplification pattern was more significant in HER2+ PDX models (Figure 12B). The 17q amplification was observed where the *ERBB2* gene located. The structure variation was notable in the TNBC subtype compared with other subtypes and the variation of chromosome 8 was outstanding where the *MYC* gene located (Figure 12C).

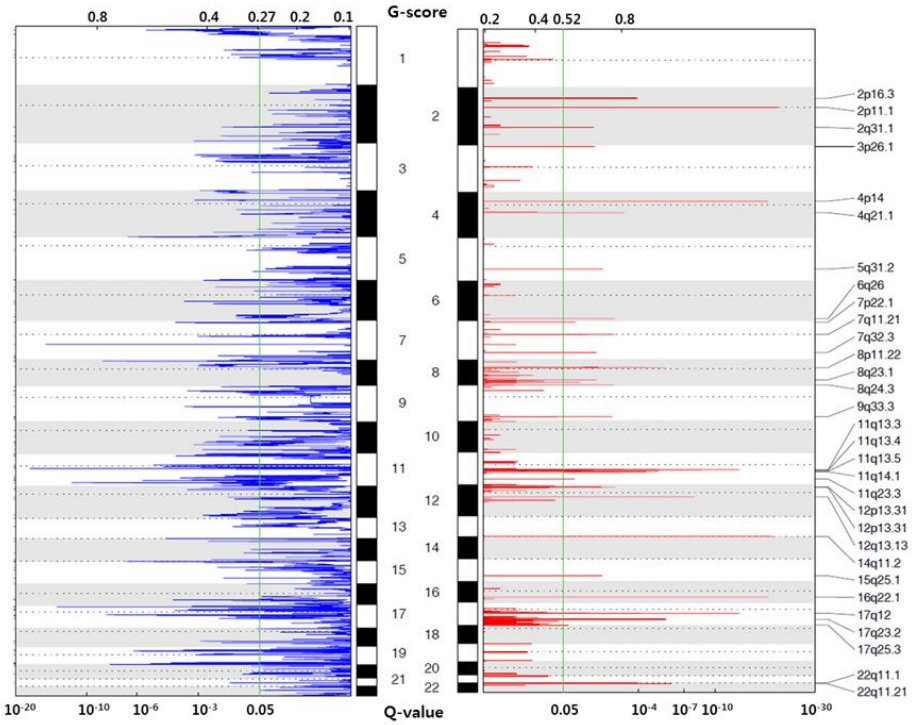

Figure 11. The copy number variation pattern of PDX model.

The copy number variation of all PDX model was illustrated in this figure. The amplified loci was written the right side of the figure.

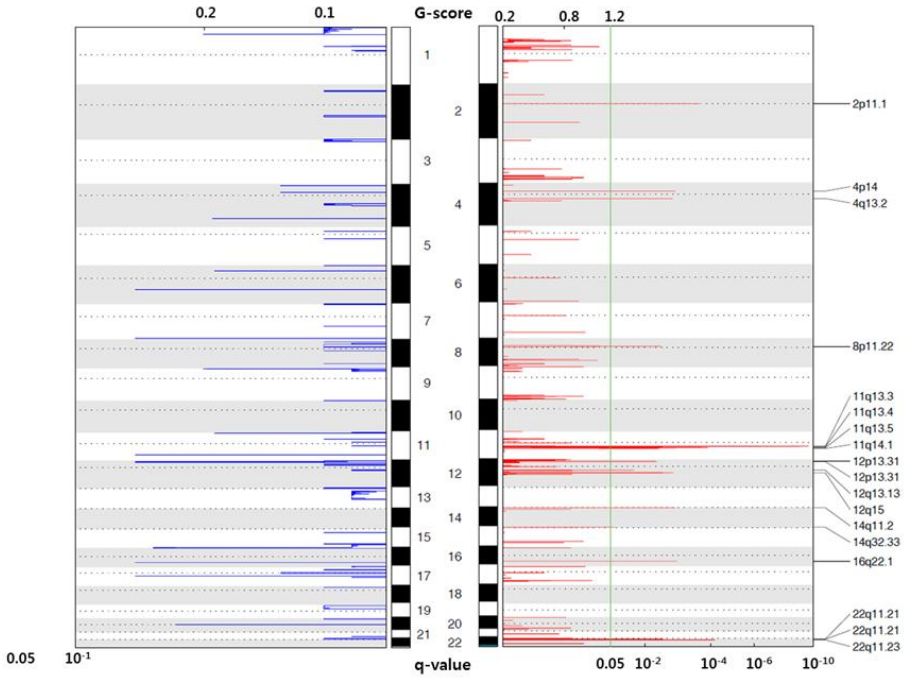

Figure 12. The copy number variation pattern of PDX model analyzed by the subtype of each samples.

A. The copy number variation of HR+ PDX model was illustrated in this figure. The amplified loci was written the right side of the figure.

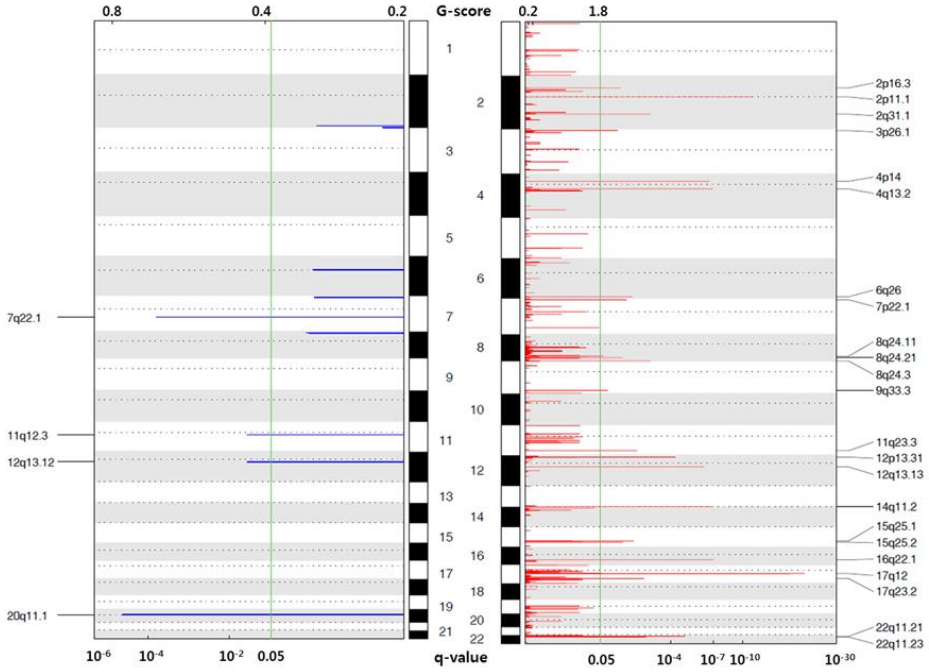

Figure 12. B. The copy number variation of HER2+ PDX model was illustrated in this figure. The significant loci was indicated.

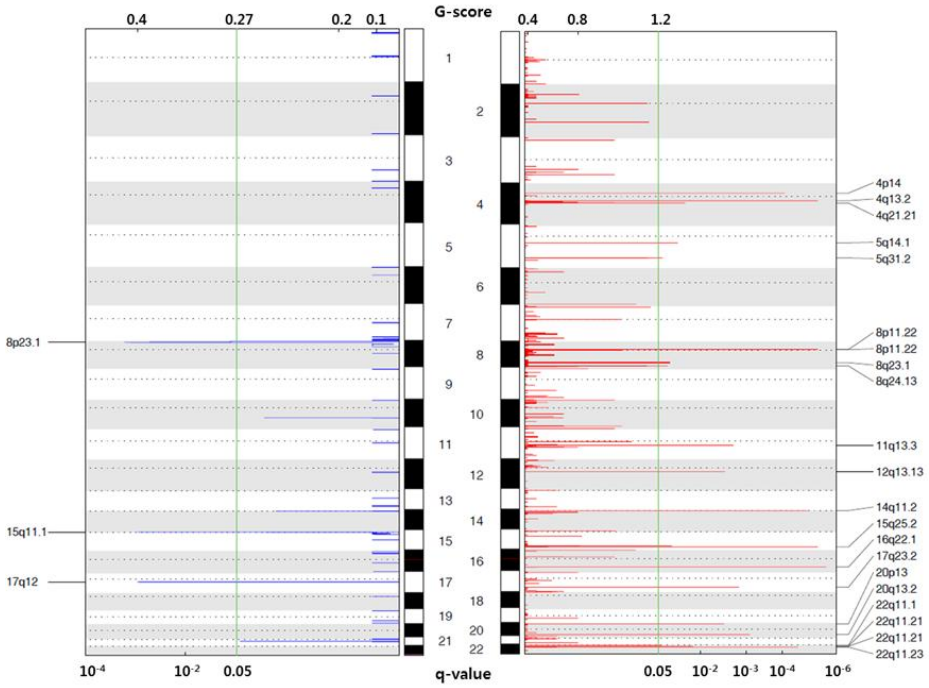

Figure 12. C. The copy number variation of the TNBC PDX model was illustrated in this figure. The significant loci was indicated.

5. The gene expression profile of the established PDX model

The RNA expression pattern was analyzed for understanding the character of the PDX model. PDX tumor tissues were used for analysis. Unsupervised hierarchical clustering results revealed that each sample was clustered by its respective subtype (Figure 13A). HR+ HER2- and HER2+ samples tend to cluster one group, whereas the TNBC samples clustered another. The samples were divided into two groups and examined which functional pathways presented differences between the two groups. G:Profiler was used for analysis and reduct ontologies using REVIGO. Elevated pathways were associated with blood vessel development, cell proliferation, cell adhesion, and extracellular matrix organization. In contrast, the pathways related to cell projection organization and hormone transport were downregulated (Figure 13B). In general, the RNA expression profile tended to cluster based on the subtype of each sample, and the proliferation and cell adhesion-related ontologies were upregulated in the TNBC dominant clustering.

Next, the RNA expression profile was examined by subtype of tumor. In comparison among subtype, the luminal A subtype was compared with other subtypes. The luminal B subtype and HER2-enriched subtype showed

elevated expression of cell cycle progression related genes compare to the luminal A subtype. Interestingly, the expression of immune response-related genes was down-regulated in both subtypes compare with the luminal A subtype (Figure 14A and 14B). The comparison of basal-like subtype and luminal A subtype showed elevated cell differentiation-related genes and reduced GTPase binding relation genes (Figure 14C).

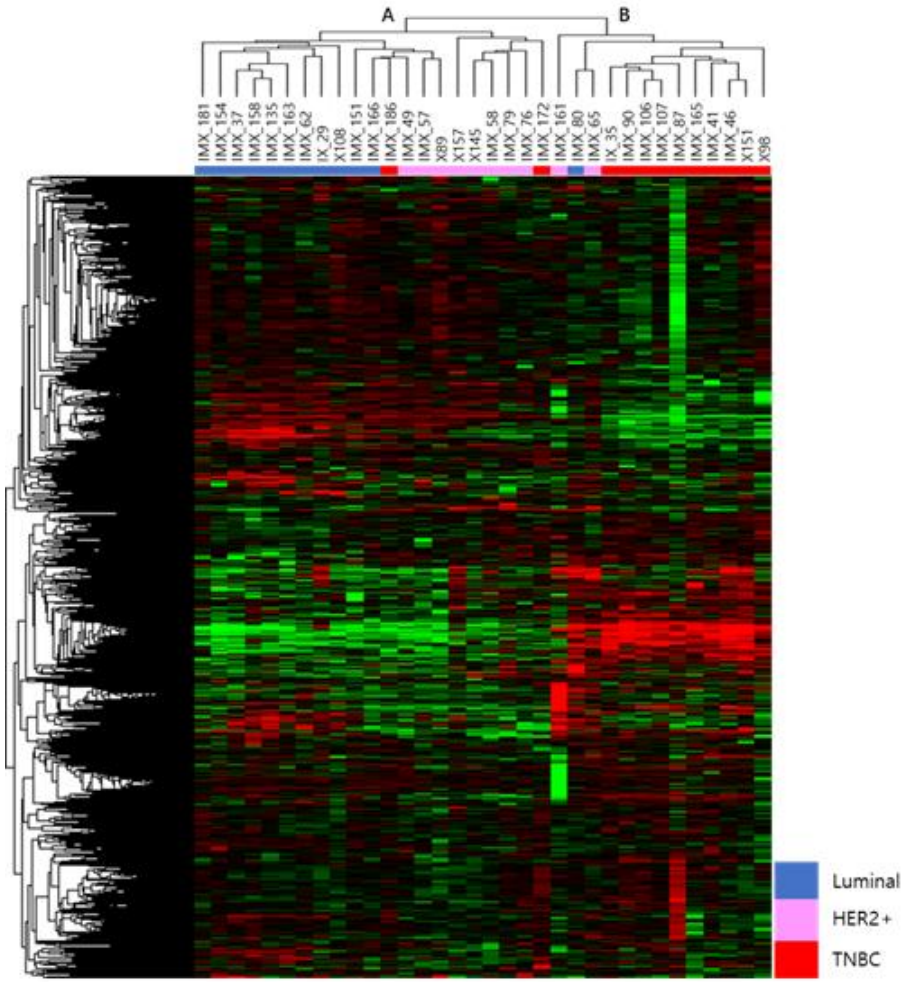

Figure 13. The Unsupervised hierarchical clustering of transcriptome data and ontology analysis.

A. Unsupervised hierarchical clustering results of the PDX model. The sample clustering pattern is similar to the sample's originate subtype. The subtype of each sample indicated below the sample name by the color. Two major difference pattern in the heat map was observed.

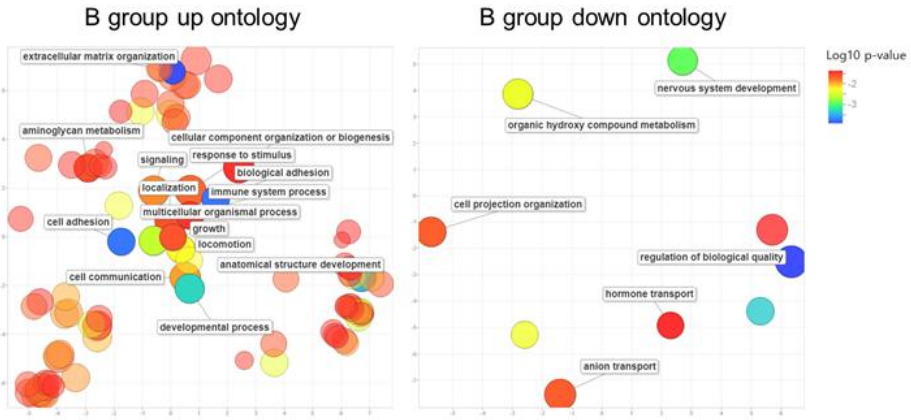

Figure 13. B. GO ontology was clustered by REVIGO. The samples were divided into two groups based on expression patterns and compare the gene ontologies. The significant ontologies were indicated in the figure.

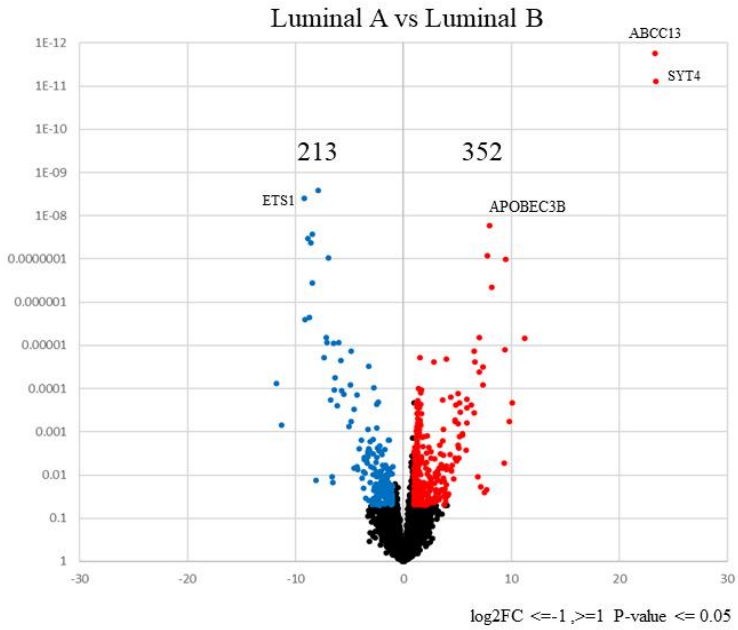

Up regulated genes

p-value	T	Q	Q&T	Q&T/Q	t type	t name
6.05E-45	776	302	85	0.281	BP	mitotic cell cycle process
9.51E-45	946	302	92	0.305	BP	mitotic cell cycle
1.09E-41	628	195	77	0.395	rea	Cell Cycle
5.56E-41	522	195	71	0.364	rea	Cell Cycle, Mitotic
8.63E-40	1249	302	98	0.325	BP	cell cycle process
3.28E-39	1766	302	114	0.377	BP	cell cycle
2.99E-30	591	302	62	0.205	BP	cell division
4.18E-28	311	302	46	0.152	BP	chromosome segregation
1.75E-27	193	302	38	0.126	CC	chromosome, centromeric region
5.84E-27	511	302	55	0.182	BP	mitotic cell cycle phase transition

Down regulated genes

p-value	T	Q	Q&T	Q&T/Q	t type	t name
2.3E-15	2165	176	64	0.364	BP	immune response
1.33E-13	24	176	11	0.062	CC	MHC protein complex
1.7E-13	975	176	41	0.233	BP	regulation of immune response
4.87E-13	1503	176	50	0.284	BP	regulation of immune system process
1.32E-12	3044	176	72	0.409	BP	immune system process
8.77E-12	16	176	9	0.051	CC	MHC class II protein complex
1.34E-11	1053	176	40	0.227	BP	positive regulation of immune system process
1.5E-11	2955	176	69	0.392	BP	cell surface receptor signaling pathway
3.3E-11	1137	176	41	0.233	BP	response to cytokine
4.75E-11	69	104	14	0.135	keg	Antigen processing and presentation

Figure 14. The comparison of gene expression by subtypes.

A. Comparison between luminal A and luminal B

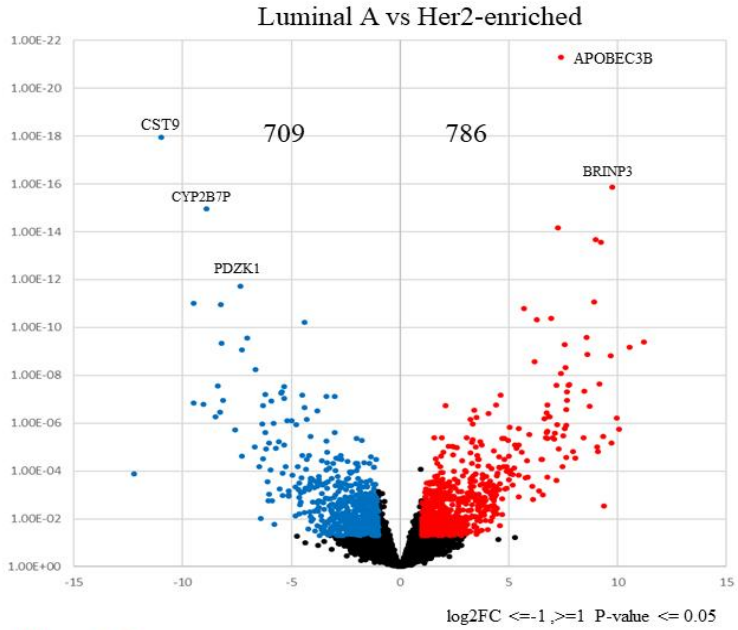

Up regulated genes

p-value	T	Q	Q&T	Q&T/Q	t type	t name
6.05E-45	776	302	85	0.281	BP	mitotic cell cycle process
9.51E-45	946	302	92	0.305	BP	mitotic cell cycle
1.09E-41	628	195	77	0.395	rea	Cell Cycle
5.56E-41	522	195	71	0.364	rea	Cell Cycle, Mitotic
8.63E-40	1249	302	98	0.325	BP	cell cycle process
3.28E-39	1766	302	114	0.377	BP	cell cycle
2.99E-30	591	302	62	0.205	BP	cell division
4.18E-28	311	302	46	0.152	BP	chromosome segregation
1.75E-27	193	302	38	0.126	CC	chromosome, centromeric region
5.84E-27	511	302	55	0.182	BP	mitotic cell cycle phase transition

Down regulated genes

p-value	T	Q	Q&T	Q&T/Q	t type	t name
2.3E-15	2165	176	64	0.364	BP	immune response
1.33E-13	24	176	11	0.062	CC	MHC protein complex
1.7E-13	975	176	41	0.233	BP	regulation of immune response
4.87E-13	1503	176	50	0.284	BP	regulation of immune system process
1.32E-12	3044	176	72	0.409	BP	immune system process
8.77E-12	16	176	9	0.051	CC	MHC class II protein complex
1.34E-11	1053	176	40	0.227	BP	positive regulation of immune system process
1.5E-11	2955	176	69	0.392	BP	cell surface receptor signaling pathway
3.3E-11	1137	176	41	0.233	BP	response to cytokine
4.75E-11	69	104	14	0.135	keg	Antigen processing and presentation

Figure 14. B. Comparison between luminal A and HER2 enriched

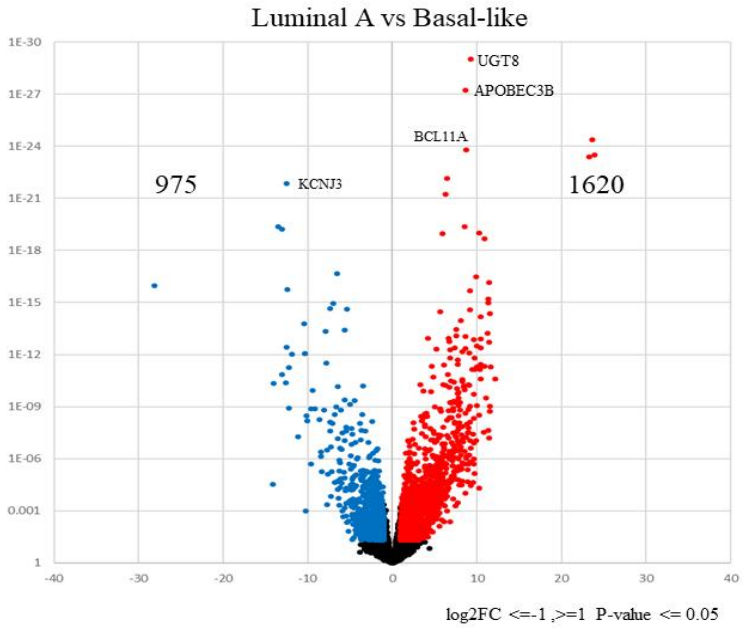

Up regulated genes

p-value	T	Q	Q&T	Q&T/Q	t type	t name
3.59E-21	12443	1355	1019	0.752	tf	Factor: ZF5; motif: NRNGNGCGCGCWN; match class: 1
1.08E-19	10314	1355	877	0.647	tf	Factor: Churchill; motif: CGGGNN; match class: 1
2.3E-18	10275	1355	869	0.641	tf	Factor: MOVO-B; motif: GNGGGGG
2.3E-18	10275	1355	869	0.641	tf	Factor: MOVO-B; motif: GNGGGGG; match class: 0
2.17E-17	6212	1329	580	0.436	BP	developmental process
1.15E-16	5793	1329	546	0.411	BP	anatomical structure development
5.15E-16	10051	1355	844	0.623	tf	Factor: AP2; motif: GCCYGSGGSN; match class: 0
5.15E-16	10051	1355	844	0.623	tf	Factor: AP2; motif: GCCYGSGGSN
5.89E-16	4088	1329	413	0.311	BP	cell differentiation
6.32E-16	4760	1329	465	0.35	BP	system development

Down regulated genes

p-value	T	Q	Q&T	Q&T/Q	t type	t name
6.33E-06	1064	783	84	0.107	BP	cellular lipid metabolic process
4.03E-05	2087	427	129	0.302	rea	Metabolism
0.000241	1399	783	97	0.124	BP	lipid metabolic process
0.000299	80	783	16	0.02	BP	peroxisome organization
0.000473	632	783	54	0.069	MF	GTPase binding
0.000541	735	427	57	0.133	rea	Metabolism of lipids
0.000563	535	783	48	0.061	MF	small GTPase binding
0.000574	258	783	30	0.038	BP	organic acid catabolic process
0.000574	258	783	30	0.038	BP	carboxylic acid catabolic process
0.00061	520	783	47	0.06	MF	Ras GTPase binding

Figure 14. C. Comparison between luminal A and basal like

6. *ESR1* mutation and *CCND1* amplification were outstanding features in the HR+ HER2- PDX model

Despite the poor success rate of generating the HR+ HER2- breast cancer PDX model in general (8), the system that used in this study revealed a marked take rate of HR+ HER2- PDX model. I focused on mutation profiling to investigate the difference in these models, thus presenting a higher establishment rate in the HR+ HER2- PDX model.

As presented in figure 8B, *ESR1* mutation is more frequent in the established HR+ HER2- PDX model. Among the 12 PDX cases, 5 harbors the oncogenic *ESR1* mutation (Figure 15). No other noticeable mutations presented subtype differences. The duration of endocrine therapy was longer in the *ESR1* mutation group compared with the *ESR1* wild-type group (median duration 45 months vs 13 months), but no statistical significance was found (Figure 16). Interestingly, *CCND1* amplification was related to *ESR1* mutation in this PDX model. *CCND1* amplification is significantly related to *ESR1* mutation by Fisher' s exact test. (Table 4, p-value = 0.0289). *CCND1* expression was further elevated in *ESR1* mutated model (Figure 17). This data suggested that the higher take rate of the HR+ HER2- PDX model is due to the higher rates of the aggressive phenotype (41.7% with *ESR1* mutation) than in previous

reports.

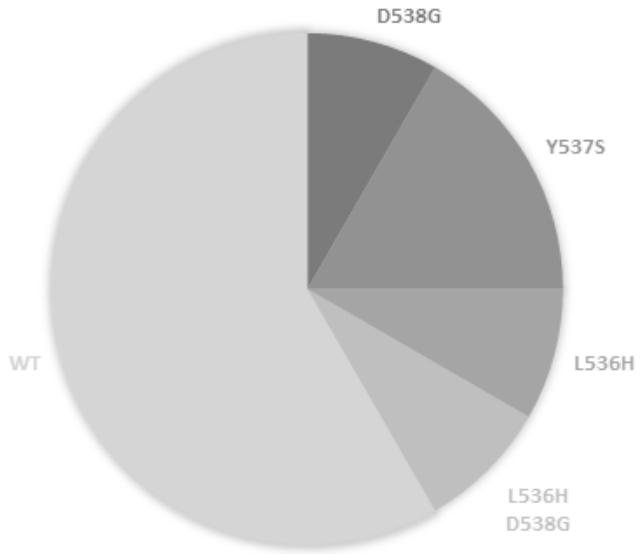

Figure 15. The population of *ESR1* mutation status in HR+ HER2- PDX model.

The *ESR1* mutation proportion in HR+ HER2- PDX model was indicated as a pie chart. The mutation site of *ESR1* was written beside the pie chart.

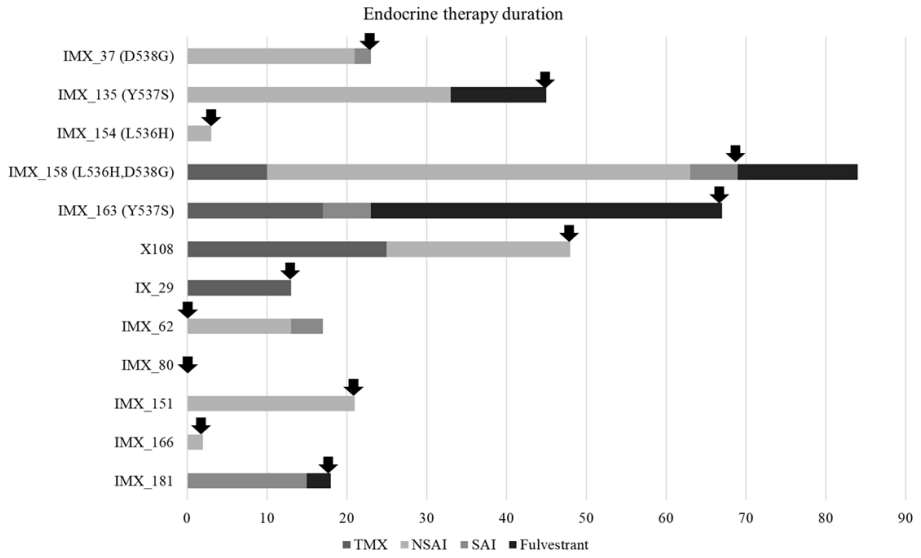

Figure 16. The endocrine therapy duration of HR+ HER2- PDX model.

The treatment duration of endocrine therapy was depicted in a bar chart. The four different drugs were used for patient treatment. The black arrow indicated the time point of biopsy for PDX transplantation. TMX: Tamoxifen, NSAI: Letrozole or Anastrozole, SAI: Exemestane.

Table 4. *CCND1* amplification and *ESR1* mutation

	***CCND1* amplification**	***CCND1* no amplification**	**P=0.0289**
***ESR1* mutant**	4	1	5
***ESR1* wild-type**	1	22	29
	11	23	34

CCND1 amplification and *ESR1* mutation were analyzed by Fisher's exact test in all of the PDX models

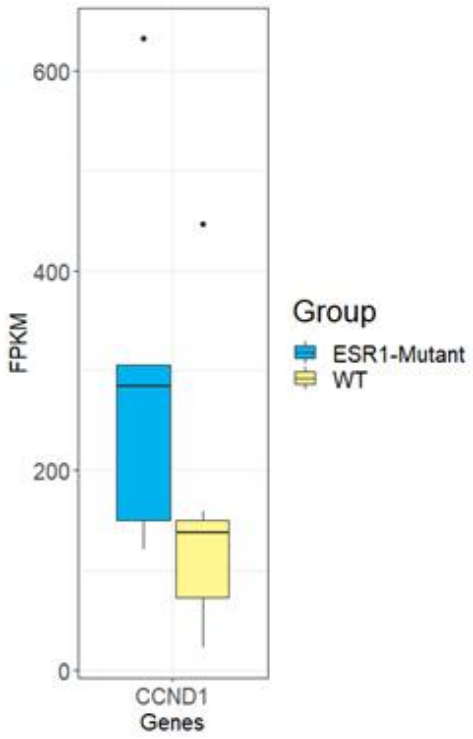

Figure 17. The relations of *CCND1* expression and *ESR1* mutation.

The FPKM value of the *CCND1* gene was analyzed and compared between the *ESR1* mutated samples and the wild type ones.

7. The IGF-1 signaling is enhanced in *ESR1* mutated HR+ HER- PDX model

Since the *ESR1* mutation is a significant feature in this HR+ HER2- PDX model, the RNA expression differences were examined in line with *ESR1* gene mutation status. As shown in figure 18, there was a clear difference in the RNA expression pattern between the two groups (Figure 18A). The gene ontology was checked for further analysis. Among several biological processes, the up-regulation of the PI3K-AKT signaling pathway was noticeable in *ESR1* mutated group (Figure 18B). To understand which factors elevated this signaling, I reviewed references. Recently, it was reported that the Insulin growth factor 1 (IGF-1) was crosstalk between IGF-1 and ERα in *ESR1* mutant cells and the PI3K-Akt axis was a major pathway of IGF-1 downstream (27, 28). Thus, it was checked that IGF-1 signaling was activated in the *ESR1* mutated PDX model. The expression patterns of IGF-1 signaling in *ESR1* mutated samples were distinguished from *ESR1* wild-type samples (Figure 19). Take all this together, *ESR1* mutation PDX samples were represented different expressions and IGF-1 signaling was elevated.

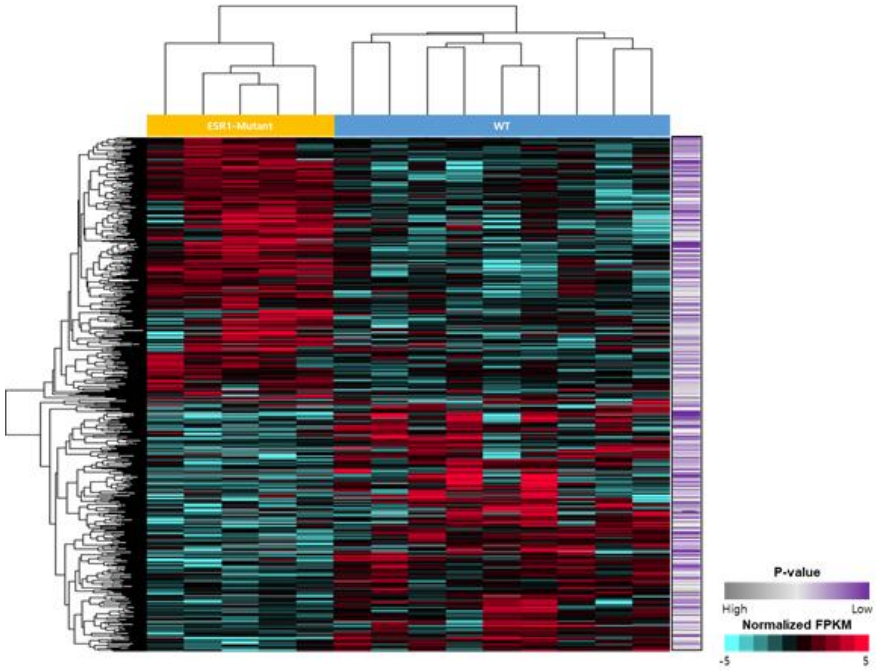

Figure 18. The RNA expression according to *ESR1* gene status.

A. The RNA expression clustering base on *ESR1* gene status.

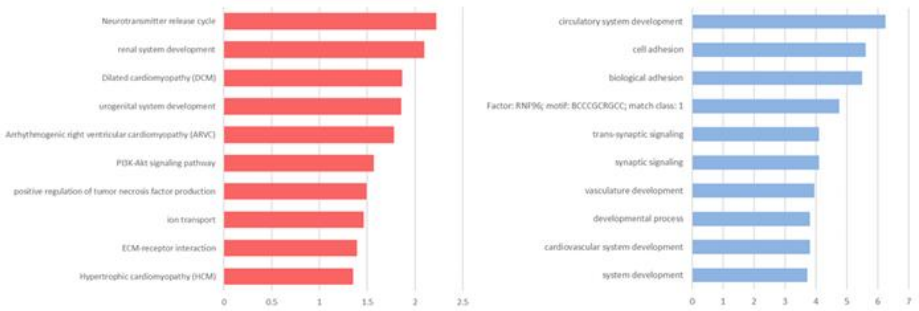

B. The gene ontology analysis results of two group by the differentially expressed genes

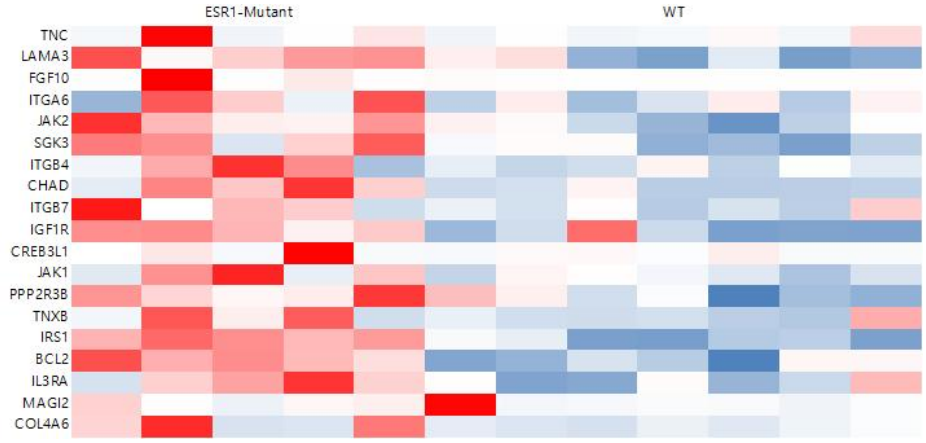

Figure 19. The elevation of IGF-1 signaling in *ESR1* mutated samples.

The heat maps of the PDX model was illustrated. The figure indicates that IGF-1 pathway-related genes differentially regulated in mutants vs wild type.

8. *APOBEC3B* expression was elevated in luminal B subtype and *PIK3CA* mutant samples

Recently, mutational signature analysis has been widely used to understand the mutation patterns and underlying biological processes. Thus, the mutational signature analysis was performed to detect whether the PDX model had a specific mutational signature. The highest and second highest signature based on cosine similarity was used for clustering. The APOBEC (COSMIC signatures 2 and 13), CpG (COSMIC signature 1), MSI (COSMIC signature 6), and BRCA (COSMIC signatures 3 and 8) signatures were prominent in this models (Figure 20). In particular, signature 3 was dominant in the TNBC subtype, whereas the APOBEC signature was prominent in HR+ HER2- subtype following signature 1 (Figure 20).

Since *APOBEC3B* is reported to promote breast cancer cell growth depending on ER (29, 30), it was analyzed the correlations between the APOBEC signature and success rate of the establishment of HR+ HER2- PDX model. Among the 12 cases of HR+ HER2- PDX, 5 cases (41.7%) had a clustered APOBEC signature. A previous study reported that *APOBEC3B* expression is associated with poor clinical outcomes and proliferative features (31). Accordingly, the APOBEC3B expression was further analyzed. Initially, it was observed that APOBEC signature samples presented a high

transcription level of APOBEC family genes. The expression level of *APOBEC3B* only showed differences among the all APOBEC family gene groups, and APOBEC group showed the highest median value (Figure 21). Next, the results of the *APOBEC3B* expression analysis revealed differences between the subtype and *PIK3CA* mutation. The transcriptome data from 34 PDX models were analyzed and then clustered by PAM 50 clustering. The *APOBEC3B* expression was the highest in TNBC, followed by luminal B, HER2, and luminal A (Figure 22). This result indicated that the HR+ HER2- PDX model presented aggressiveness. The relationships between the APOBEC activity and *PIK3CA* mutations have been reported in a previous study (32). In this PDX model, all *PIK3CA* mutant cases clustered in the APOBEC signature except one case. Moreover, the *PIK3CA* mutated samples presented a high expression of *APOBEC3B* than the wild type samples (Figure 23). Therefore, the HR+ HER2- PDX model showed APOBEC relates signature and also elevated expression of *APOBEC3B. PIK3CA* mutation seems to have relations with signature 2 and 13, and also the expression of *APOBEC3B.*

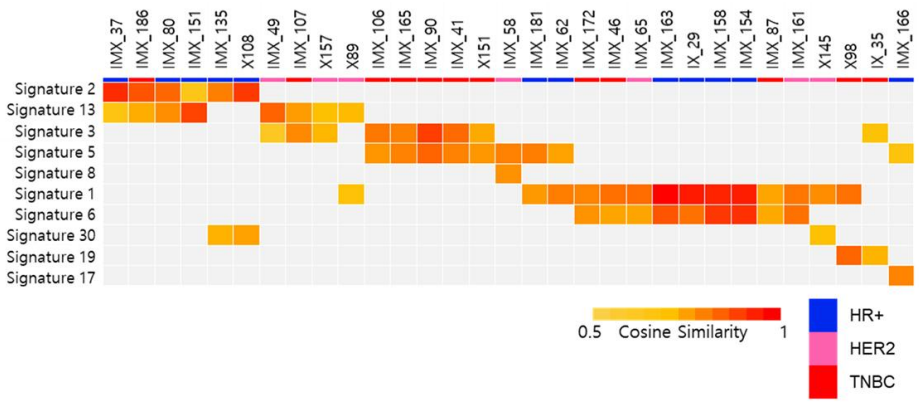

Figure 20. Mutation signature of PDX model.

Mutation signature analysis was performed and clustered. The signature depicts the 1st and 2nd highest cosine similarity. The subtype of each model was placed by the color bar below the sample names.

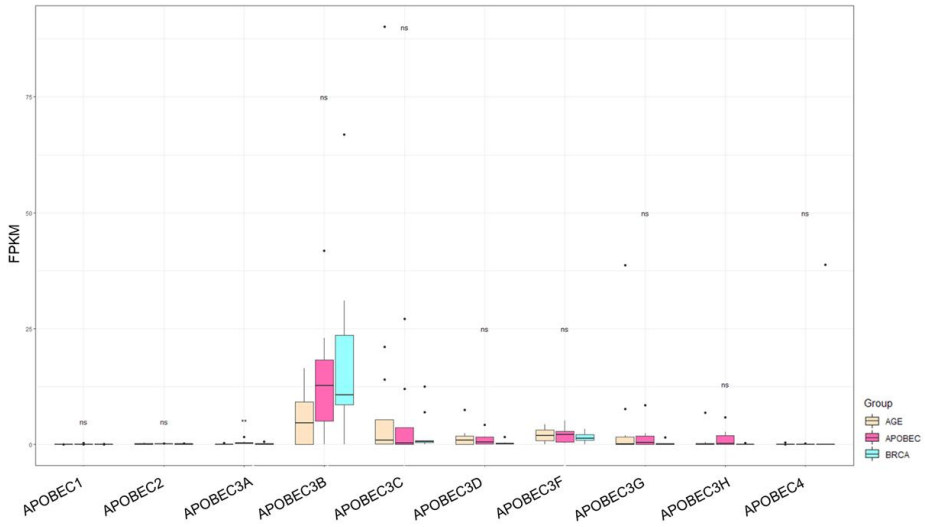

Figure 21. The expression of APOBEC family genes.

The expression of the APOBEC family gene was illustrated with its FPKM values by the signature group. *APOBEC1, APOBEC2, APOBEC3A, APOBEC3B, APOBEC3D, APOBEC3F, APOBEC3G, APOBEC3H,* and *APOBEC4* expressions were indicated with a bar graph.

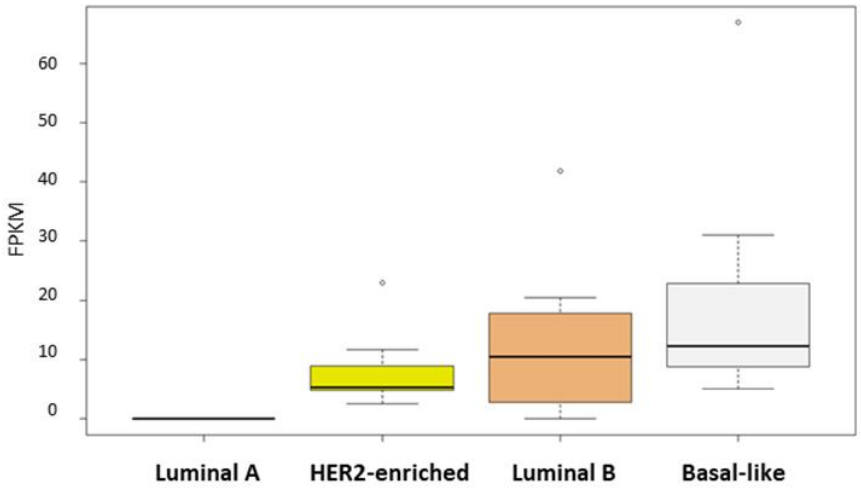

Figure 22. The elevated expression of *APOBEC3B* in luminal B subtype.

APOBEC3B expression was illustrated with its FPKM values by values by subtype. Basal-like subtype showed the highest median value and the luminal B subtype was the next.

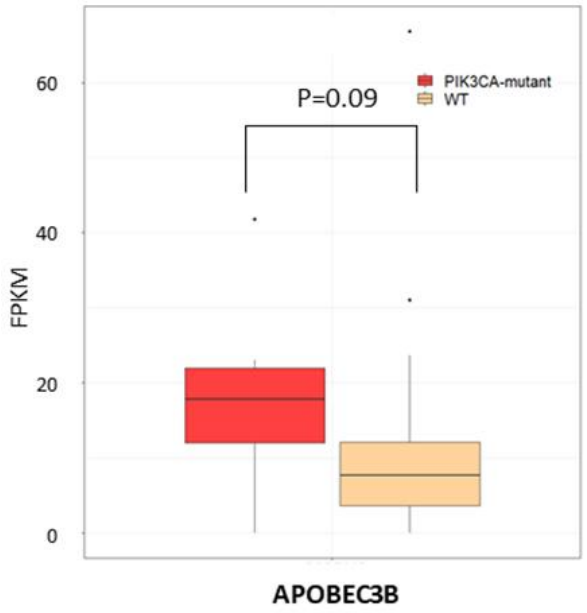

Figure 23. The elevated expression of APOBEC3B in PIK3CA mutated samples.

The expression of *APOBEC3B* was illustrated with its FPKM values according to their *PIK3CA* mutation status of each sample. The P-value of each cluster was written in the figure.

9. Comparison of genomic profiles of PDX models established at different times from the same patient

In this study, it was able to construct a PDX model using biopsy tissue obtained at different time points from the same patient. Genomic profiles of 10 PDX models from 5 different patients were compared to determine if the genomic profile was different according to the time point at which biopsy tissue was obtained. The biopsy timings and model names of the tissues were arranged in the table 5. When comparing the mutational burden between two PDX models obtained from the same patient, it was confirmed that there was no significant difference in the mutational burden, except for the case of patient #3 (Figure 24). The difference in time between biopsy tissues used in this analysis ranged from as little as 2 months to up to 22 months, and the interval between differences between biopsy points did not correlate with the mutational burden. Cancer driver mutations identified in each patient's first PDX model were also identified in the second PDX model. Additionally, genomic profile changes were confirmed using X89 and IMX_102 models with HR+ HER2- subtype. The mutation pattern of the PDX model X89, constructed at the time of resistance to various HER2 targeted therapies, and the IMX_102 model, constructed at the time of resistance to

various chemotherapy, were compared. The distribution of the mutational pattern between the two models was similar (Figure 25A). In addition, as a result of confirming the change of the non-silent somatic mutation between samples, it was confirmed that it has 130 identical somatic mutations, although some differences were seen (Figure 25B). In particular, cancer-related mutation identified in the first model was the same in the second model. The copy-number variation between the two models was similar (Figure 26). Therefore, this data indicate that PDX models constructed at different time points have the same genomic profile.

Table 5. The list of PDX model and biopsy site information from the same patient tumor tissue

Patient	Sample	DATE	Biopsy site	
Patient #1	X89	20140721	Metastatic tumor	skin
	IMX_102	20160503	Metastatic tumor	skin
Patient #2	IMX_151	20170118	Metastatic tumor	Lt SCN
	IMX_160	20170329	Metastatic tumor	Lt SCN
Patient #3	IMX_163	20170410	Metastatic tumor	liver
	IMX_185	20170904	Metastatic tumor	liver
Patient #4	IMX_139	20161013	Primary tumor	breast
	IMX_165	20170428	Primary tumor	breast
Patient #5	IMX_183	20170714	Primary tumor	breast
	IMX_186	20170922	Primary tumor	breast

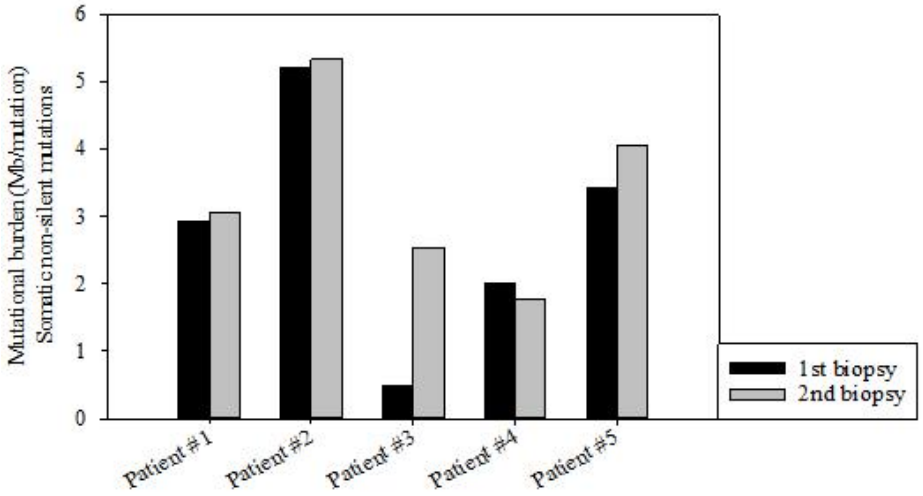

Figure 24. Comparison of the mutational burden of PDX models established from the same patient at different time points.

The mutational burden of 10 PDX models established form 5 different patients were demonstrated. Each case was labeled with patient number.

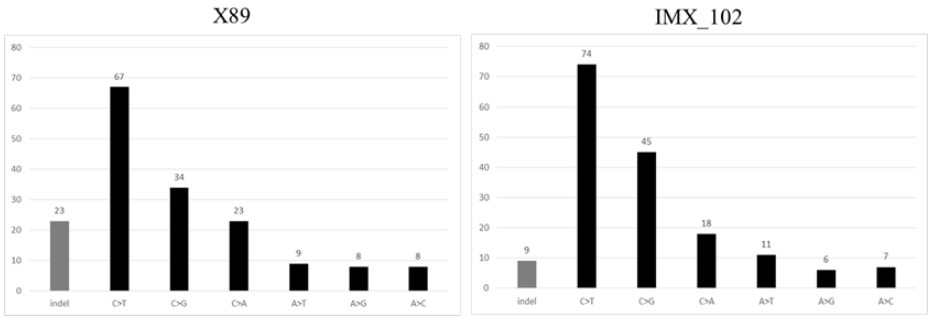

Figure 25. The comparison of mutation pattern and somatic mutation between X89 and IMX_102 model.

A. The mutation pattern of X89 model and IMX_102 model was demonstrated. The Y axis indicates the count of each mutation.

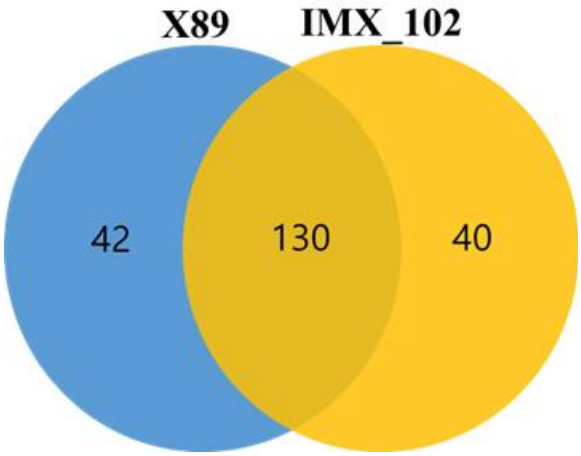

B. The number of somatic mutations found in both samples.

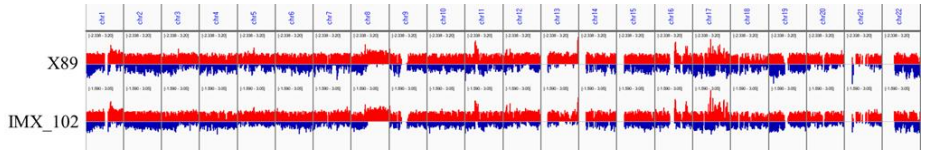

Figure 26. The comparison of CNV pattern between X89 and IMX_102 model.

The CNV pattern of X89 model and IMX_102 model was demonstrated as a bar chart. The chromosome numbers were written in the top of the chart.

10. The clinical implication of the PDX model

After the genomic profiling of the established PDX model, the clinical application of this model establishment and the utility of genomic analysis of the PDX model was examined.

To demonstrate that PDX genomic profiling can predict the clinical outcome of a disease, it was analyzed the genetic feature of IMX-158 case originated from a metastatic liver specimen of a patient who received various endocrine therapies. The IMX-158 PDX model harbored two *ESR1* mutation sites in L536H and D538G (Figure 27A) with *CCND1* amplification (Figure 27B). The donor of IMX-158 model was treated with fulvestrant and CDK4/6 inhibitor (palbociclib). After 4 months of treatment, the patient achieved partial response (Figure 28). The maximal standardized uptake value (SUV) with PDG PET/CT was reduced from 8.6 to 6.0 in the liver and 6.8 to 2.5 in the pelvic bone during the treatment. At 15 months, the disease progressed in the previously noted bone lesion (maximal SUV from 3.6 to 5.1). Compared to the result of phase III PALOMA-3 trial with median PFS of 9.5 months (95% CI 9.2-11.0 months) in fulvestrant plus palbociclib group (33, 34), the patient had longer PFS and this data suggested that *CCND1* amplification and *ESR1* mutation might affect the longer benefit from the treatment. Moreover, the genomic

analysis of the PDX model may facilitate the treatment choice and interpretation of the clinical outcome of a certain treatment.

The X89 model was established from ER expressed HER2 type tumor. The donor of X89 was treated with several anti-HER2 therapies including trastzumab, lapatinib, and margetuximab (MGAH22). The WES data of the PDX model revealed *ERBB2* amplification similar to the patient data (Figure 29A). Moreover, this model conferred somatic mutation of *ATR* E1986K and *BRCA2* E1734K (Figure 29B, Table 6). The biological function was not reported initially in these two mutations; however, they revealed to play a pivotal role in the DNA repair pathway. Thus, we tried to adjust the ATR inhibitor in this model to evaluate the drug efficacy. PDX tumor growth was delayed in the ATR inhibitor treatment group when compared with the vehicle group (Figure 30). These results indicated that the administration of ATR inhibitor to the ATR mutated tumor could be a good treatment option. Also, PDX models could be a useful tool for the test *in vivo* drug sensitivity and could be strong evidence to expand the drug' s clinical indications.

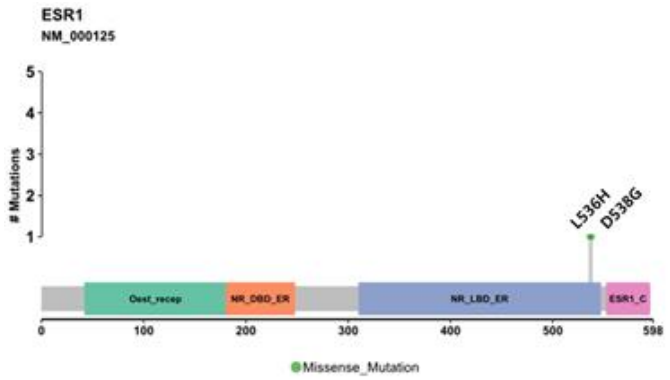

Figure 27. The *ESR1* mutation and *CCND1* amplification observed in the IMX-158 model.

A. *ESR1* mutation site and its domain of IMX-158 sample were illustrated.

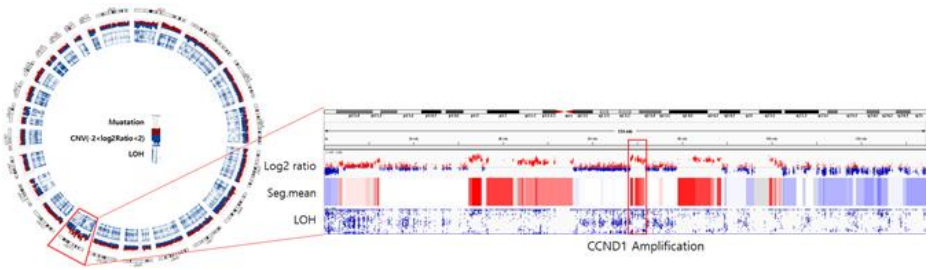

B. The circos plot of IMX-158 sample which depicts the CNV of this sample.

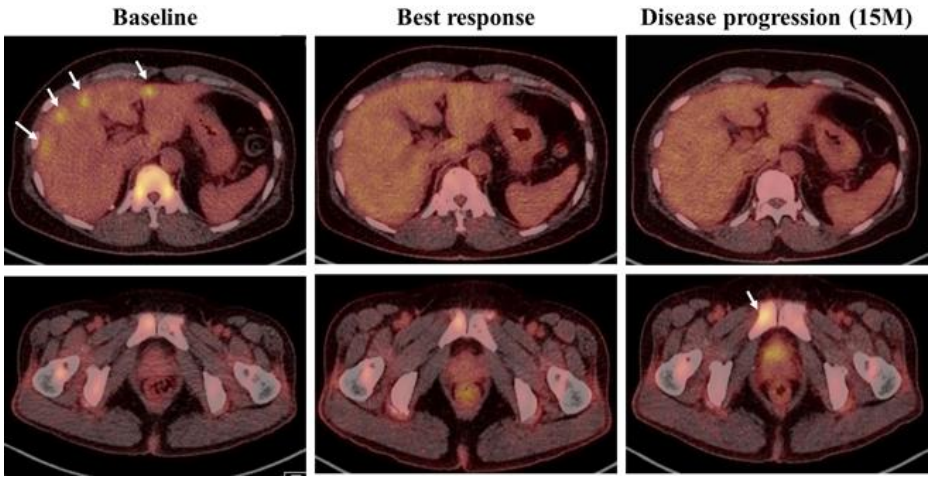

Figure 28. The response of treatment of fulvestrant and palbociclib to the donor patient.

PET scan image of the donor of the IMX-158 sample. Baseline indicates the time before the initiation of palbociclib and fulvestrant treatment. The best response was seen four months later from baseline. White arrows indicate the hypermetabolic lesions in the liver and pelvic bone.

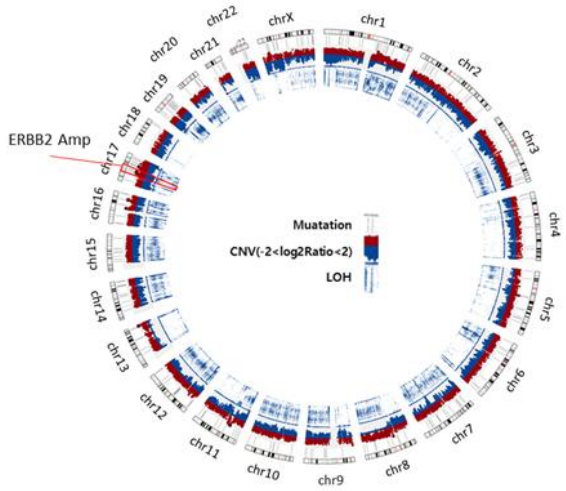

Figure 29. The *ATR* mutation and *ERBB2* amplification observed in the X89 model.

A. The circos plot of X89 sample which depicts the CNV of this sample.

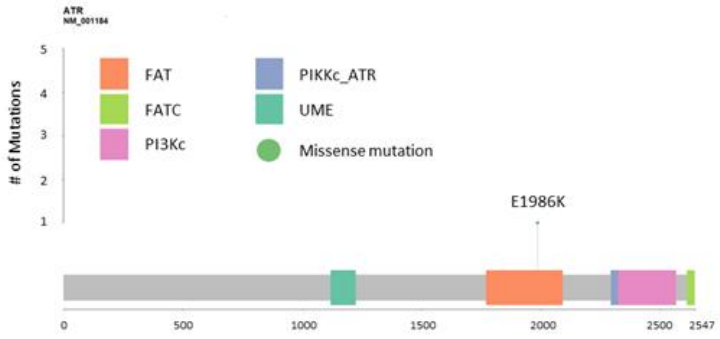

B. *ATR* mutation site and its domain of the X89 sample were illustrated.

Table 6. Mutation and CNV status of X89 PDX model

Subtype	Mutation		Amplification	
	Germline gene	Somatic gene	Gene	Cytoband
ILC	CHK2	PIK3CA	ERBB2	17q21
	MTOR	ATR	CD44	11p13
	TSC2	TSC2	MYC	8q
	FGFR2	BRCA2		

The histologic subtype of implant tissue, germline mutation gene list, somatic mutation gene list, and the amplified gene list was indicated in this table. The somatic mutation of *ATR* and *BRCA2* ware revealed by WES.

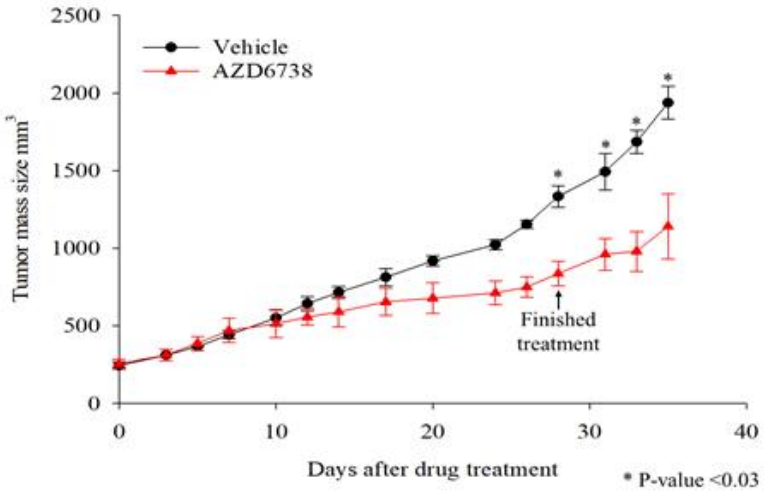

Figure 30. The tumor growth delay effect by treatment of ATR inhibitor in the X89 PDX model.

The X89 PDX model was treated with ATR inhibitor, AZD6738, for 4 weeks. The mouse models were monitored extra one week. The tumor volumes were presented by a graph.

DISCUSSION

Breast cancer is highly heterogeneous, not only across the patient population but also in intra-tumoral features. The NGS technique has been previously used to understand the behavior of breast cancer, and the genomic alterations in tumorigenesis or tumor progression have been extensively described; however, these efforts focused only on early breast cancer (24, 35). Although several mutation profiles of mBC are available (26), they are insufficient to completely understand the breast cancer characteristics. Moreover, numerous novel agents have revealed outstanding responses compared to those used previously, but the response rate to systemic chemotherapy is about 50% to 90% for primary tumors (36). Thus, it is essential to reveal the genomic profile of metastatic tissue and to explore an efficient therapeutic strategy for the patient with mBC.

The PDX model is known to play a pivotal role in retaining the molecular and biological features of the donated tumor tissue (8). The CNV and exome sequencing data present high fidelity between the paired samples (6). Moreover, drug efficacy tests using the PDX model have shown promising results; cetuximab and gemcitabine have been shown to present similarity in drug activity and

clinical trial data (37-39). Nevertheless, the PDX model has certain limitations. As not all the PDX implantation leads to PDX model establishment, improvement of the PDX take rate is a big issue. Especially, because of the low take rate of the HR+ HER2- PDX model, reports analyzing genomic and ethnic diversity in HR+ HER2- model is not sufficient yet.

In this study, we report a take rate of 26% using core needle biopsy specimens. (Figure 1). In contrast to previous studies (6, 7, 40, 41), the take rate of HR+ HER2- PDX model in our system significantly high (22%). The enrolled patients of this study were mBC patients which considered an aggressive form of breast cancer. Among established PDX models, 67.6% of donor tumor tissues were histology grade 3. In addition, we tried to set up an efficient and rapid system to establish PDX models. Most (86%) of fresh tumor biopsy tissues were delivered to the implant team within 30 minutes and implanted within an hour. Thus, these factors might have affected the elevated take rate in this PDX transplantation system.

The model fidelity was analyzed between the paired tumor tissues from donor and from PDX model. The tumor subtype based on the IHC result showed 90% concordant (Figure 4B). The somatic mutation and CNV fidelity between the donor and PDX model were also well matched (Figure 5

and Figure 6). The take rate of the proliferative tumor was higher in this PDX model (Figure 3). Also, further analysis of the Ki-67 index also showed that established HR+ HER2- PDX model was observed higher Ki-67 index compared with the fail cases (Figure 31). The PDX model presented a high frequency of *TP53* and *ESR1* mutations, as well as a high tumor mutation burden compared with other metastatic regimens. The somatic mutation allele frequency tended to strengthen in the PDX model. This might occur due to clonal composition changes or as a result of increased human tumor DNA purity in the PDX model (6).

The reason for the successful-establishment of the HR+ HER2- PDX model was further analyzed. Initially, I focused on *ESR1* mutation in the luminal subtype. Among 12 HR+ PDX models, 5 cases harbored *ESR1* mutation (41%). Moreover, all mutations founded in HR+ HER2- PDX model were known pathogenic mutations (L536H, Y537S, D538G). Except for one case, all patients were previously treated with multiple lines of endocrine therapy from 23 months to 84 months. The PDX model harboring the *ESR1* mutation also harbored *CCND1* amplification in four of the five cases (Table 4), and the expression of *CCND1* differed from the *ESR1* wild-type samples. All these features implied that this HR+ HER2- PDX model had aggressive characteristics. The tumor tissues were obtained from locally advanced/and or metastatic breast cancer patients, and this might be the

cause of the aggressive phenotype of HR+ HER2- models compared to the various previous literature. Unfortunately, this hypothesis could not validate due to tissue shortage for further analysis. As the amount of the needle biopsy specimen was limited, it was not available to remain tumor tissue for the failed cases.

APOBEC signature and the high expression of *APOBEC3B* were prevalent in the PDX model. HR+ HER2- PDX model clustered into the aging- and APOBEC-related signatures, and the mutation patterns were also matched. Moreover, *APOBEC3B* expression was upregulated in the luminal subtype and *PIK3CA* mutated samples. The *PIK3CA* mutation samples were clustered into signatures 2 and 13. The relationship between APOBEC signature and PIK3CA mutation is well reported, but that between APOBEC gene expression and mutational signature remains unclear. From the recent report of Cescon DW et al., the *APOBEC3B* expression is related to a lack of ER expression and also related to the expression of key proliferation-associated genes (*AURKA, MK167,* and *CCNB1*) (29, 31). Based on these data, we surmised that the metastatic tissue of HR+ HER2- tumors tend to have a more aggressive phenotype; thus, the take rate of the HR+ HER2- PDX is higher than that of the previous reports.

The PDX model can be efficiently used for translational

research. IMX-158, an ER+ HER2- breast cancer model, harbors *ESR1* mutation and *CCND1* amplification. *ESR1* D538G mutation was reported to promote estrogen-independent activation of the estrogen receptor (42). Moreover, mBCs with *ESR1* mutation showed a worse prognosis and were less responsive to aromatase inhibitors (43). However, this mutation elicits a response to fulvestrant treatment in mouse models and clinical trials (44). Besides the *ESR1* mutation, *CCND1* amplification might also affect treatment decisions. Cyclin D1 is a binding partner of CDK4/6 and regulates the cell cycle in G1 cell cycle (45), which is the target of palbociclib. Cyclin D1 is a transcriptional target of the ER (46) and the amplification of *CCND1* is founded in 15% of breast cancer (47). Moreover, over 50% of breast cancer overexpress cyclin D1 (47). Response to palbociclib was associated with cyclin D1 expression in cell lines (48). Based on these studies, the donor of this model was treated with fulvestrant and palbociclib. This patient could enjoy prolonged progression-free survival (PFS) of 15 months, which is longer than the median PFS in the PALOMA-3 trial, 9.5 months (95% CI 9.2-11.0 months). This case highlights the potential that genomic analysis of the PDX model could be utilized for treatment selection and prediction of clinical outcomes. Moreover, the PDX genomic profile and the PDX model itself can contribute to the translational research. In

the drug tests using X89, an HR- HER2+ PDX model, genomic analyses of the PDX model could be used to expand the drug's indication to the unknown somatic mutations. These results also implicate that the PDX models could be helpful to test *in vivo* sensitivity of specific drugs, and could provide some evidence to facilitate the clinical application to the real patients.

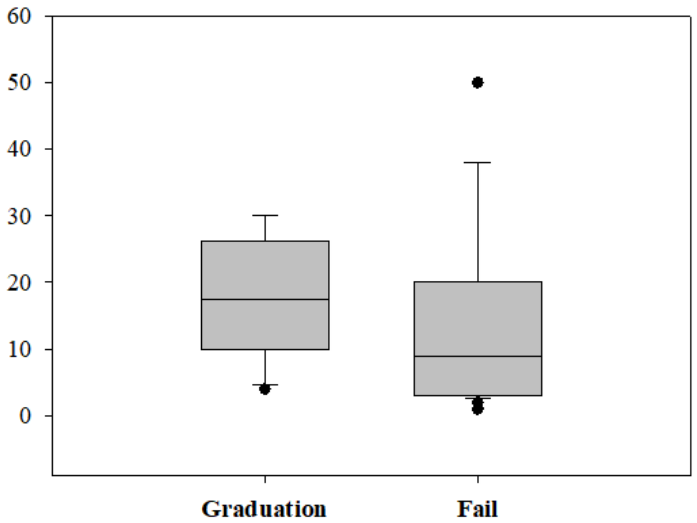

Figure 28. The comparison of Ki-67 value in established PDX samples.

The median value of Ki-67 among graduation and failed PDX models. The value of Ki-67 was examined the donor tissues.

CONCLUSION

The hormone-positive breast cancer PDX model is well established in this study. The genomic profile of the PDX tissue well reflects the character of the donor tissue. *ESR1* mutation, *CCND1* amplification, and APOBEC3B signature, which represent the aggressive phenotype, is outstanding in the HR+ HER2- PDX model. Moreover, the PDX model established in this study proved the potential to utilize clinical implications.

ACKNOWLEDGEMENTS

I would like to thank Dongjin shin who help to this study for bioinformatics analysis. I am also grateful to professor Jong-Il Kim and Minjung Kim for supervised bioinformatics analysis. I also had the great pleasure of working with professor Charles Lee, Deukchae NA, and the member of his laboratory for helping the PDX model establishment. I would like to acknowledge the assistance of Kyung-Hun Lee, Tae-Yong Kim, and Han-Byeol Lee for patient tissue collection. I also gratefully acknowledge the help of Yaewon Yang, Go-Un Woo, and Dae-Won Lee for patient characteristic analysis. I would like to extend my deepest gratitude to Ahrum Min for supporting this study. Finally, I would like to express my deepest appreciation to my professor, Seock-Ah Im for advising and supporting this study.

REFERENCES

1. Kang SY, Kim YS, Kim Z, Kim HY, Kim HJ, Park S, et al. Breast Cancer Statistics in Korea in 2017: Data from a Breast Cancer Registry. J Breast Cancer. 2020;23(2):115-28.
2. Vuong D, Simpson PT, Green B, Cummings MC, Lakhani SR. Molecular classification of breast cancer. Virchows Arch. 2014;465(1):1-14.
3. Koren S, Bentires-Alj M. Breast Tumor Heterogeneity: Source of Fitness, Hurdle for Therapy. Mol Cell. 2015;60(4):537-46.
4. Longley DB, Johnston PG. Molecular mechanisms of drug resistance. J Pathol. 2005;205(2):275-92.
5. Press JZ, Kenyon JA, Xue H, Miller MA, De Luca A, Miller DM, et al. Xenografts of primary human gynecological tumors grown under the renal capsule of NOD/SCID mice show genetic stability during serial transplantation and respond to cytotoxic chemotherapy. Gynecol Oncol. 2008;110(2):256-64.
6. Hidalgo M, Amant F, Biankin AV, Budinska E, Byrne AT, Caldas C, et al. Patient-derived xenograft models: an emerging platform for translational cancer research. Cancer Discov. 2014;4(9):998-1013.
7. Yu J, Qin B, Moyer AM, Sinnwell JP, Thompson KJ, Copland JA, 3rd, et al. Establishing and characterizing

patient-derived xenografts using pre-chemotherapy percutaneous biopsy and post-chemotherapy surgical samples from a prospective neoadjuvant breast cancer study. Breast Cancer Res. 2017;19(1):130.

8. Dobrolecki LE, Airhart SD, Alferez DG, Aparicio S, Behbod F, Bentires-Alj M, et al. Patient-derived xenograft (PDX) models in basic and translational breast cancer research. Cancer Metastasis Rev. 2016;35(4):547-73.

9. Li H, Durbin R. Fast and accurate short read alignment with Burrows-Wheeler transform. Bioinformatics. 2009;25(14):1754-60.

10. do Valle IF, Giampieri E, Simonetti G, Padella A, Manfrini M, Ferrari A, et al. Optimized pipeline of MuTect and GATK tools to improve the detection of somatic single nucleotide polymorphisms in whole-exome sequencing data. BMC Bioinformatics. 2016;17(Suppl 12):341.

11. Cibulskis K, Lawrence MS, Carter SL, Sivachenko A, Jaffe D, Sougnez C, et al. Sensitive detection of somatic point mutations in impure and heterogeneous cancer samples. Nat Biotechnol. 2013;31(3):213-9.

12. Karczewski KJ, Weisburd B, Thomas B, Solomonson M, Ruderfer DM, Kavanagh D, et al. The ExAC browser: displaying reference data information from over 60 000 exomes. Nucleic Acids Res. 2017;45(D1):D840-D5.

13. Auer PL, Johnsen JM, Johnson AD, Logsdon BA, Lange LA, Nalls MA, et al. Imputation of exome sequence

variants into population- based samples and blood-cell-trait-associated loci in African Americans: NHLBI GO Exome Sequencing Project. Am J Hum Genet. 2012;91(5):794-808.

14. Genomes Project C, Auton A, Brooks LD, Durbin RM, Garrison EP, Kang HM, et al. A global reference for human genetic variation. Nature. 2015;526(7571):68-74.

15. Krumm N, Sudmant PH, Ko A, O'Roak BJ, Malig M, Coe BP, et al. Copy number variation detection and genotyping from exome sequence data. Genome Res. 2012;22(8):1525-32.

16. Rosenthal R, McGranahan N, Herrero J, Taylor BS, Swanton C. DeconstructSigs: delineating mutational processes in single tumors distinguishes DNA repair deficiencies and patterns of carcinoma evolution. Genome Biol. 2016;17:31.

17. Alexandrov LB, Nik-Zainal S, Wedge DC, Aparicio SA, Behjati S, Biankin AV, et al. Signatures of mutational processes in human cancer. Nature. 2013;500(7463):415-21.

18. Dobin A, Davis CA, Schlesinger F, Drenkow J, Zaleski C, Jha S, et al. STAR: ultrafast universal RNA-seq aligner. Bioinformatics. 2013;29(1):15-21.

19. Anders S, Pyl PT, Huber W. HTSeq--a Python framework to work with high-throughput sequencing data. Bioinformatics. 2015;31(2):166-9.

20. Parker JS, Mullins M, Cheang MC, Leung S, Voduc D,

Vickery T, et al. Supervised risk predictor of breast cancer based on intrinsic subtypes. J Clin Oncol. 2009;27(8):1160-7.
21. Love MI, Huber W, Anders S. Moderated estimation of fold change and dispersion for RNA-seq data with DESeq2. Genome Biol. 2014;15(12):550.
22. Reimand J, Arak T, Adler P, Kolberg L, Reisberg S, Peterson H, et al. g:Profiler-a web server for functional interpretation of gene lists (2016 update). Nucleic Acids Res. 2016;44(W1):W83-9.
23. Supek F, Bosnjak M, Skunca N, Smuc T. REVIGO summarizes and visualizes long lists of gene ontology terms. PLoS One. 2011;6(7):e21800.
24. Cancer Genome Atlas N. Comprehensive molecular portraits of human breast tumours. Nature. 2012;490(7418):61-70.
25. Wagle N, Painter C, Anastasio E, Dunphy M, McGillicuddy M, Kim D, et al. The Metastatic Breast Cancer (MBC) project: Accelerating translational research through direct patient engagement. Journal of Clinical Oncology. 2017;35.
26. Lefebvre C, Bachelot T, Filleron T, Pedrero M, Campone M, Soria JC, et al. Mutational Profile of Metastatic Breast Cancers: A Retrospective Analysis. PLoS Med. 2016;13(12):e1002201.
27. Li Z, Levine KM, Bahreini A, Wang P, Chu D, Park BH, et al. Upregulation of IRS1 Enhances IGF1 Response in

Y537S and D538G ESR1 Mutant Breast Cancer Cells. Endocrinology. 2018;159(1):285-96.
28. Creighton CJ, Casa A, Lazard Z, Huang S, Tsimelzon A, Hilsenbeck SG, et al. Insulin-like growth factor-I activates gene transcription programs strongly associated with poor breast cancer prognosis. J Clin Oncol. 2008;26(25):4078-85.
29. Kanu N, Cerone MA, Goh G, Zalmas LP, Bartkova J, Dietzen M, et al. DNA replication stress mediates APOBEC3 family mutagenesis in breast cancer. Genome Biol. 2016;17(1):185.
30. Periyasamy M, Patel H, Lai CF, Nguyen VTM, Nevedomskaya E, Harrod A, et al. APOBEC3B-Mediated Cytidine Deamination Is Required for Estrogen Receptor Action in Breast Cancer. Cell Rep. 2015;13(1):108-21.
31. Cescon DW, Haibe-Kains B, Mak TW. APOBEC3B expression in breast cancer reflects cellular proliferation, while a deletion polymorphism is associated with immune activation. Proc Natl Acad Sci U S A. 2015;112(9):2841-6.
32. Henderson S, Chakravarthy A, Su X, Boshoff C, Fenton TR. APOBEC-mediated cytosine deamination links PIK3CA helical domain mutations to human papillomavirus-driven tumor development. Cell Rep. 2014;7(6):1833-41.
33. Turner NC, Huang Bartlett C, Cristofanilli M. Palbociclib in Hormone-Receptor-Positive Advanced Breast Cancer. N Engl J Med. 2015;373(17):1672-3.

34. Cristofanilli M, Turner NC, Bondarenko I, Ro J, Im SA, Masuda N, et al. Fulvestrant plus palbociclib versus fulvestrant plus placebo for treatment of hormone-receptor-positive, HER2-negative metastatic breast cancer that progressed on previous endocrine therapy (PALOMA-3): final analysis of the multicentre, double-blind, phase 3 randomised controlled trial. Lancet Oncol. 2016;17(4):425-39.
35. Ellis MJ, Ding L, Shen D, Luo J, Suman VJ, Wallis JW, et al. Whole-genome analysis informs breast cancer response to aromatase inhibition. Nature. 2012;486(7403):353-60.
36. Li Z, Kang Y. Emerging therapeutic targets in metastatic progression: A focus on breast cancer. Pharmacol Ther. 2016;161:79-96.
37. Bertotti A, Migliardi G, Galimi F, Sassi F, Torti D, Isella C, et al. A molecularly annotated platform of patient-derived xenografts ("xenopatients") identifies HER2 as an effective therapeutic target in cetuximab-resistant colorectal cancer. Cancer Discov. 2011;1(6):508-23.
38. Julien S, Merino-Trigo A, Lacroix L, Pocard M, Goere D, Mariani P, et al. Characterization of a large panel of patient-derived tumor xenografts representing the clinical heterogeneity of human colorectal cancer. Clin Cancer Res. 2012;18(19):5314-28.
39. Garrido-Laguna I, Uson M, Rajeshkumar NV, Tan AC,

de Oliveira E, Karikari C, et al. Tumor engraftment in nude mice and enrichment in stroma- related gene pathways predict poor survival and resistance to gemcitabine in patients with pancreatic cancer. Clin Cancer Res. 2011;17(17):5793-800.

40. Goetz MP, Kalari KR, Suman VJ, Moyer AM, Yu J, Visscher DW, et al. Tumor Sequencing and Patient-Derived Xenografts in the Neoadjuvant Treatment of Breast Cancer. J Natl Cancer Inst. 2017;109(7).

41. Zhang X, Claerhout S, Prat A, Dobrolecki LE, Petrovic I, Lai Q, et al. A renewable tissue resource of phenotypically stable, biologically and ethnically diverse, patient-derived human breast cancer xenograft models. Cancer Res. 2013;73(15):4885-97.

42. Toy W, Weir H, Razavi P, Lawson M, Goeppert AU, Mazzola AM, et al. Activating ESR1 Mutations Differentially Affect the Efficacy of ER Antagonists. Cancer Discov. 2017;7(3):277-87.

43. Angus L, Beije N, Jager A, Martens JW, Sleijfer S. ESR1 mutations: Moving towards guiding treatment decision-making in metastatic breast cancer patients. Cancer Treat Rev. 2017;52:33-40.

44. Reinert T, Saad ED, Barrios CH, Bines J. Clinical Implications of ESR1 Mutations in Hormone Receptor-Positive Advanced Breast Cancer. Front Oncol. 2017;7:26.

45. Weinberg RA. The retinoblastoma protein and cell cycle control. Cell. 1995;81(3):323-30.
46. Kwapisz D. Cyclin-dependent kinase 4/6 inhibitors in breast cancer: palbociclib, ribociclib, and abemaciclib. Breast Cancer Res Treat. 2017;166(1):41-54.
47. Cadoo KA, Gucalp A, Traina TA. Palbociclib: an evidence-based review of its potential in the treatment of breast cancer. Breast Cancer (Dove Med Press). 2014;6:123-33.
48. Finn RS, Dering J, Conklin D, Kalous O, Cohen DJ, Desai AJ, et al. PD 0332991, a selective cyclin D kinase 4/6 inhibitor, preferentially inhibits proliferation of luminal estrogen receptor-positive human breast cancer cell lines in vitro. Breast Cancer Res. 2009;11(5):R77.

국문 초록

유방암은 여성에게 가장 흔한 암으로 조기에 발견될 경우 예후가 좋지만, 전이성 유방암의 경우 질병 자체가 복잡한 성격을 띠고 있으며, 환자의 생명을 위협하는 질병이다. 분자생물학적인 연구를 통하여 여러 표적 치료제들이 개발되면서 전이성 유방암 환자의 생존 기간이 연장되고 있으나, 저항성 기전으로 인하여 질병이 다시 악화하는 것을 경험하고 있고, 이러한 어려움을 극복하려는 다양한 시도가 진행되고 있다. 암 환자 유래 조직 이식 동물모델 (patient-derived xenograft: PDX) 은 표적 치료제를 포함하는 항암 치료에 대한 공여자의 임상 결과를 예측하는 모델로 활용될 수 있고, 해당 모델을 이용하여 새로운 항암제의 효능을 입증하기 위한 동물모델로써 활용할 수도 있다. 최근까지 유방암의 환자 유래 조직 이식 동물모델은 대부분 서양인의 원발성 유방암 조직을 이용하여 수립되었다. 따라서 본 연구에서는 한국인 전이성 유방암 환자의 PDX 모델을 확립하고, 수립된 동물모델의 종양 조직을 이용하여 PDX 모델의 유전자 특성을 확인하며, 해당 유전적 특성이 있는 동물모델에서 효과가 있는 표적 치료제의 적응증을 확인하여 임상시험에 활용하는 가능성을 알아보고자 한다.

전이성 유방암 환자에서 경피적 생검 조직을 채취하여 NSG 마우스에 이식하였고 마우스에서 증식한 종양 조직을 이용하여 유전체 분석을 시행하였다. 유전자 변이 및 RNA 발현 양상을 확인하기 위하여 차세대 염기서열 분석 기법을 이용하여 whole-exome sequencing과 transcriptome sequencing을 수행하였고 유전자 복제수 변이와 종양 돌연변이 부담을 분석하였다. 또한, 등록된 환

자의 임상 기록을 검토하여 전이성 유방암 환자의 임상적 요인과 병리학적 요인을 정리하여 수립된 PDX 모델의 분자생물학적 특성 및 유전체 분석결과와 비교 분석하였다. 또한, PDX 모델을 이용하여 표적 치료제의 항종양 효과를 관찰하였다.

전체 130명 환자에서 획득한 151개의 종양 조직이 이종이식에 활용되었다. 전체 151건의 사례 중 40건의 PDX 모델이 수립되어 26.5 %에서 PDX가 수립되었다. PDX 수립 성공률을 호르몬 수용체와 HER2 성장인자 수용체 발현 정도에 따라 아형을 나누어 분석하였고, 각 아형에서의 성공률 또한 20%를 초과함을 확인하였다. 특히, 기존에 성공률이 낮았던 호르몬 수용체 양성 아형에서도 22%의 성공률을 보였다. 본 연구에서 수립된 PDX 모델은 공여자의 종양 조직과 동일한 조직학적 특성을 보였다. 또한, 유전자 변이 및 유전자 복제 변이의 정도도 PDX 모델과 공여자 조직간 유사한 패턴을 나타내었다. *TP53, PIK3CA, ESR1* 및 *GATA3* 유전자의 돌연변이가 PDX 표본에서 빈번하게 발생함을 확인하였다. 이러한 유전자의 변이는 공여자의 조직에서 확인된 것과 같이 PDX 모델에서도 확인하였으며, 유전자 변이 빈도가 PDX 모델에서 증가함을 확인하였다. 본 연구에서 수립된 PDX 모델 중, 호르몬 수용체 양성 아형의 경우 *ESR1* 유전자 변이와 *CCND1* 유전자 증폭이 흔히 관찰되었고, APOBEC signature가 CpG signature와 함께 보임을 확인하였다. *ESR1* 유전자의 변이와 *CCND1* 유전자 증폭의 특성을 동시에 지니는 동물모델의 공여자에서 에스트로겐 수용체 분해제인 fulvestrant과 CDK4/6 억제제인 palbociclib을 병용 투여하여 임상 반응을 확인하여 PDX 모델에서 분석한 유전체 정보를 환자의 치료에 활용할 수 있었다. 또한, *ATR* 유전자 변이가 있는 동물모델에서 ATR 억제제인 AZD6738을 투여하여 종양 성장

억제 효과가 있음을 확인하였다.

본 연구에서 전이성 유방암 환자의 종양 조직을 이용하여 효과적으로 PDX 모델을 수립하였다. 특히 본 연구에서는 호르몬 수용체 양성 아형에서도 22%의 높은 성공률도 PDX 모델이 수립되었다. PDX 모델의 유전체 특성은 공여자의 조직에서 보이는 유전체 특성을 잘 반영하고 있음을 확인하였고, 이러한 유전체 특성을 이용하여 임상에서 환자의 치료 전략 수립에 도움이 될 수 있음을 입증하였다. 이러한 결과를 통하여 PDX 모델의 수립이 중개 의학 연구에서 활용 가능성을 제시하였다.

주요어: 전이성 유방암, 환자 유래 조직 이식 동물모델, Whole exome sequencing, 중개 의학 연구, 한국인 PDX 모델

학번: 2014-31286